LATVIAN
JOURNAL
of
PHYSICS
and TECHNICAL
SCIENCES

ISSN 0868 - 8257

2

(Vol. 59)

2022

CONTENTS

LATVIAN
JOURNAL
of
PHYSICS
and TECHNICAL
SCIENCES

LATVIJAS
FIZIKAS
un TEHNISKO
ZINĀTŅU
ŽURNĀLS

ЛАТВИЙСКИЙ
ФИЗИКО-
ТЕХНИЧЕСКИЙ
ЖУРНАЛ

Published six times a year since February 1964
Iznāk sešas reizes gadā kopš 1964. gada februāra
Выходит шесть раз в год с февраля 1964 года

2 (Vol. 59) • 2022

RĪGA

Language Editor: O. Ivanova
Computer Designer: I. Begicevs

INDEXED (PUBLISHED) IN

www.scopus.com
www.sciendo.com
EBSCO (Academic Search Complete, www.epnet.com), INSPEC (www.iee.org.com).
VINITI (www.viniti.ru), Begell House Inc/ (EDC, www.edata-center.com).

Issuers: Institute of Physical Energetics,
Institute of Solid State Physics, University of Latvia
Registration Certificate Number: 000700221

Editorial Contacts:
14 Dzerbenes Street, Riga, LV - 1006
Ph.: + 371 67551732
E-mail: leo@lza.lv
www.fei-web.lv

LATVIAN JOURNAL OF PHYSICS
AND TECHNICAL SCIENCES
2022, N 2

DOI: 10.2478/lpts-2022-0007

LATTICE DYNAMICS CALCULATIONS FOR $Mg_{1-x}Zn_xO$ SOLID SOLUTIONS

*C. F. Tipaldi, J. Gabrusenoks

Institute of Solid State Physics, University of Latvia,
8 Kengaraga Str., Riga, LV-1063, LATVIA
*e-mail: tipaldi@cfi.lu.lv

In this study, $Mg_{1-x}Zn_xO$ solid solutions are studied by modelling lattice dynamics, using the methods of classical molecular dynamics. These time-efficient methods are of great interest since they allow using large crystallic structures, which reduce artificial defect periodicity. The main program used is General Utility Lattice Program (*GULP*). The Buckingham potential is used for modelling interatomic forces. The parameters for this potential are found for different effective ionic charges by using lattice parameters and vibrational frequencies obtained from *ab initio* calculations performed in the program *CRYSTAL14*. With these potentials, the dispersion relations and densities of states have been calculated for MgO, ZnO and $Mg_{1-x}Zn_xO$. Calculations have been made for different Mg and Zn contents in the wurtzite and cubic phase solid solutions, respectively, using the supercell method and a large number of Brillouin zone sampling points.

New interatomic potentials for interactions Mg-O, O-O, Zn-O have been obtained. These potential parameters have been verified and the phonon dispersion curves and DOS for MgO and ZnO utilising these potential parameters have been compared to other studies, both experimental and theoretical. By adding more Zn in the cubic phase (c-MgO) solution, no local vibrational modes are observed; however, there is a clear spectral widening and a noticeable change in the low frequency region (100–300 cm^{-1}) of the DOS. Adding more Mg in wurtzite phase (w-ZnO) solution, on the other hand, results in local vibrational modes in the mid (350 cm^{-1}) and high frequency (650 cm^{-1}) regions.

Keywords: *Concentration, crystals, lattice dynamics, MD calculations, solid solutions, structure.*

1. INTRODUCTION

Theoretical calculations can be used for description of crystal lattice dynamics. There are multiple determination methods of accuracy and efficiency. Some, such as *ab initio,* calculations are done from fundamental quantum mechanical principles and are remarkably accurate, but these require large amounts of computation power and time. Other methods, such as classical molecular dynamics (MD), are done using classical approximations and these require much less time; however, their accuracy can be limited and is highly dependent on the interatomic potential functions [1].

A great deal of interest has recently arisen around the solid solution of ZnO and MgO denoted as $Mg_{1-x}Zn_xO$ [2]–[6]. These have applications in optoelectronic devices, such as UV detectors, since the band gap of $Mg_{1-x}Zn_xO$ is variable by the component of each constituent metal in the solid solution and it ranges from 3.37 eV (wurtzite phase) to 7.8 eV (cubic phase). The research of this material is multifaceted, but this study specifically concerns lattice dynamics and phonon spectra. The vibrational information of a material is useful in order to inquire about a multitude of its properties.

One important issue with theoretical lattice dynamics calculations is artificial defect periodicity, which arises because supercells are used to describe the structure and their size is limited by computing power and time restrictions. The main goal here is to use the time-efficient classical MD and supercell methods to obtain phonon spectra for $Mg_{1-x}Zn_xO$ of many different Mg and Zn concentrations.

2. THEORY

MgO and ZnO are inorganic, nonmetallic compounds. MgO in normal conditions forms a FCC rock-salt structure (Fig. 1) with space group symmetry *Fm3m* (No. 225) [7], [8]. The chemical bond between Mg and O is mostly ionic with some covalency. ZnO in normal conditions forms a wurtzite structure (Fig. 2) with space group symmetry $P6_3mc$ (No. 186) [7], [8]. Zn and O form a semi-ionic and semi-covalent bond. The two oxides can be dissolved into one another by using vacuum annealing methods. In the literature, it has been established that Mg dissolves in w-ZnO up to about 33 %, while Zn dissolves in c-MgO up to about 50 % [2]–[4], [9].

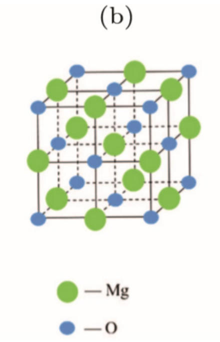

Fig. 1. c-MgO structure.

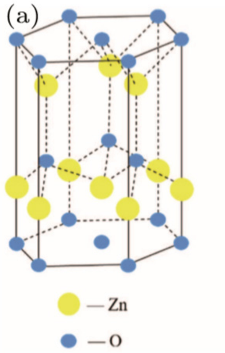

Fig. 2. w-ZnO structure.

Classical MD calculations are based upon energy minimisation for a given structure. The crystal lattice is described by point masses representing the atoms connected by springs representing the chemical bonds. Each interatomic bond is described by a potential function, which describes the dependency of potential energy from the interatomic distance. Such functions are many but one of the most popular and the one used in the work is the Buckingham potential, which is in the form [10]:

$$\boldsymbol{V(r) = A\exp(-\rho r) - \frac{C}{r^6}}\,.$$

The Buckingham potential describes both attraction and repulsion between the atoms, which are due to the Coulomb electrostatic forces and the Pauli exclusion principle [11]. Furthermore, a core-shell model is used for the oxygen atoms. In order to properly describe the lattice dynamics of a structure, the appropriate energy minimum must be found for the structure and it requires the fitting of the potential function to some input values. Such input values are the lattice parameters, phonon modes and frequencies, elastic constants etc. For the Buckingham potential, the parameters that require fitting are $\boldsymbol{A, \rho, C}$, the core-shell interaction requires fitting the constant $\boldsymbol{k}$ and, in addition, the charges of the cores and shells of ions involved in the Coulomb interaction are necessary.

The calculations in this work were done using two programs – *CRYSTAL14* [12], [13] for *ab initio* calculations and *General Utility Lattice Program* (*GULP*) [14], [15] for classical MD calculations. *Ab initio* calculations in this work were used in order to obtain input data for *GULP*. The input data consisted of lattice parameters of the oxides and their phonon modes and frequencies in the Γ point of the first Brillouin zone.

The method is such:

1. In *CRYSTAL14*, the structures of MgO and ZnO are found (lattice parameters) and their Γ point phonon modes calculated.
2. Using these input data in *GULP*, the interatomic potential parameters are fitted for metal-oxygen and oxygen-oxygen bonds.
3. Using the fitted potentials, the phonon DOS and dispersion for MgO and ZnO are calculated and compared to the literature.
4. For the $Mg_{1-x}Zn_xO$ solid solutions, supercells are constructed and optimized for every different Mg and Zn component.
5. Phonon DOS are calculated for each solid solution, multiple configurations checked for one arbitrary concentration.

In *CRYSTAL14*, the *ab initio* calculations are done using DFT with the functional B3LYP. The Gaussian type atomic basis sets for the elements can be found on the *CRYSTAL* website [16].

The interatomic potential fitting in *GULP* requires some initial parameters to be input in the program. These initial Buckingham potential parameter values for the Mg-O, Zn-O and O-O interactions were taken from the literature – the work of Lewis and Catlow [17], where they published their potential parameters for c-MgO, and the dissertation of Binks [18], where potential parameters for w-ZnO were given – and the fitting done from there. Effective ionic charges, however, were fitted manually by approximating the experimental MgO and ZnO LO and TO phonon frequencies in the ***Γ point***. These were split in two because the electric charge and the chosen ionic charge dictated the amount of splitting. Concerning the $Mg_{1-x}Zn_xO$ solid solutions, the choice of potential parameters was to use the obtained O-O interaction parameters from c-MgO for the cubic phase of $Mg_{1-x}Zn_xO$ and O-O interaction parameters from w-ZnO for the wurtzite phase of $Mg_{1-x}Zn_xO$.

3x3x3 supercells were used for Mg_4O_4 and Zn_2O_2, yielding structures of 216 and 108 atoms, respectively. The configurations of the atoms were set using a random number generator. For DOS calculations, 8000 BZ **k** points were sampled for MgO and 15625 **k** points for ZnO in order to achieve the same spectral resolution. All of the dynamics calculations were done at a constant temperature of 0 K and pressure of 0 Pa.

3. RESULTS AND DISCUSSION

The potential fitting yielded new parameters for the interactions in the c-MgO and w-ZnO structures (Tables 1 and 2). The ionic charges were chosen as 1.6e for both metal cores and 0.87e and -2.47e for the core and shell of oxygen, respectively.

Table 1. Fitted Parameters for MgO

	A, eV	ρ, Å	C, eV*Å	from, Å	to, Å	k, eV/Å²
Mg-O	29208.28	0.182	0.000001	0.0	8.0	
O-O	184.74	0.448	0.000072	0.0	12.0	79.48

Table 2. Fitted Parameters for ZnO

	A, eV	ρ, Å	C, eV*Å	from, Å	to, Å	k, eV/Å²
Zn-O	1136.82	0.296	0.046	0.0	8.0	
O-O	8663.60	0.440	7031.16	0.0	12.0	30.03

The obtained potential parameters were verified by performing calculations for phonon DOS and dispersion in MgO and ZnO. The obtained DOS and dispersion curves (Figs. 3 and 4) were compared to those found in the literature.

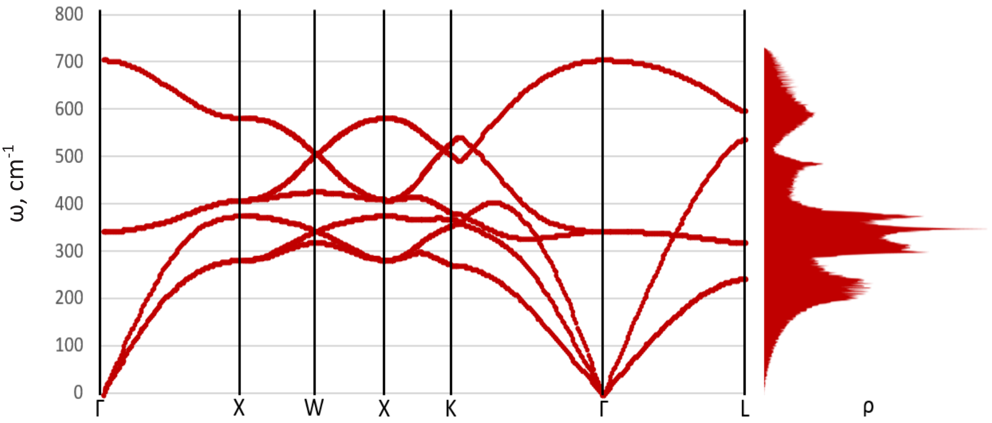

Fig. 3. Phonon DOS and dispersion in MgO using classical MD, from this study.

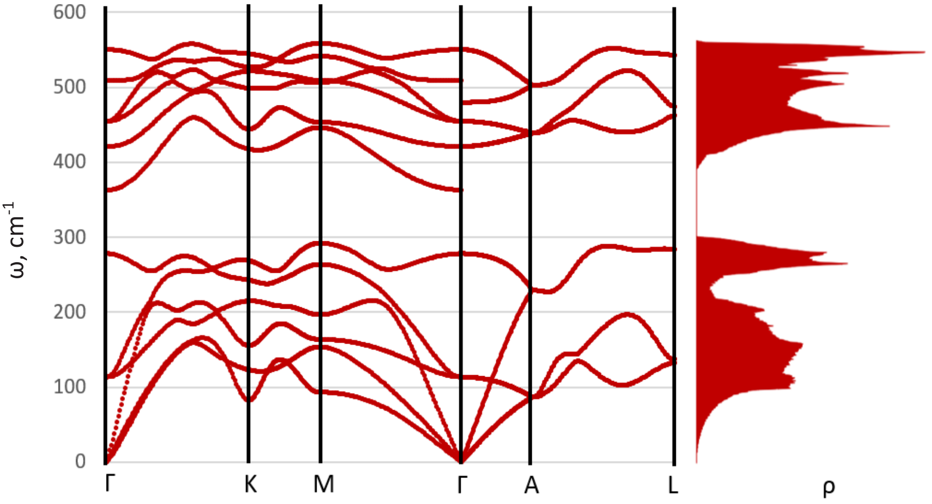

Fig. 4. Phonon DOS and dispersion in ZnO using classical MD, from this study.

The phonon dispersion and DOS of MgO were compared to the study of Al-Qasir et al. [19], specifically Fig. 3 where phonon dispersion and DOS curves were obtained both from *ab initio* calculations and neutron scattering. The phonon properties of ZnO were compared to the study done by Mankad et al. [20], specifically Fig. 4 showing dispersion and DOS curves for bulk ZnO.

In these comparisons, it was observed that the potential parameters had enough accuracy to describe in a realistic manner the lattice dynamics of the two oxides. The frequency values at BZ symmetry points were close in both comparisons between works. While there were some differences in the phonon dispersion curves in each of the comparisons, the overall nature and main characteristics of these dispersions were similar. The phonon DOS in both cases showed a larger similarity. The differences might in part be due to the different effective ionic charges used in each calculation which was also due to the lack of a charge fitting algorithm available in the program *GULP*. In spite of those differences, however, it was decided that the potentials were credible enough and could be used for further calculations.

The main calculations in this work concerned the phonon DOS of the $Mg_{1-x}Zn_xO$ solid solution. For this purpose, supercells were constructed for cubic and wurtzite structures and different solute concentrations were dissolved in these structures.

For the cubic phase of $Mg_{1-x}Zn_xO$, the Zn concentrations (x) used were:
0.0000 (0 atoms), 0.0093 (1 atom),
0.0648 (7 atoms), 0.1296 (14 atoms),
0.2500 (27 atoms).

For the wurtzite $Mg_{1-x}Zn_xO$ phase, the Zn concentrations (x) used were:
1.0000 (54 atoms), 0.9815 (53 atom),
0.9444 (51 atoms), 0.8704 (47 atoms),
0.7407 (40 atoms), 0.5000 (27 atoms).

The upper limits for concentrations were chosen by observing when the solid solution transformed into a mixed-phase upon optimization. At around 33 % Zn contenty, the cubic structure started to deform and change.

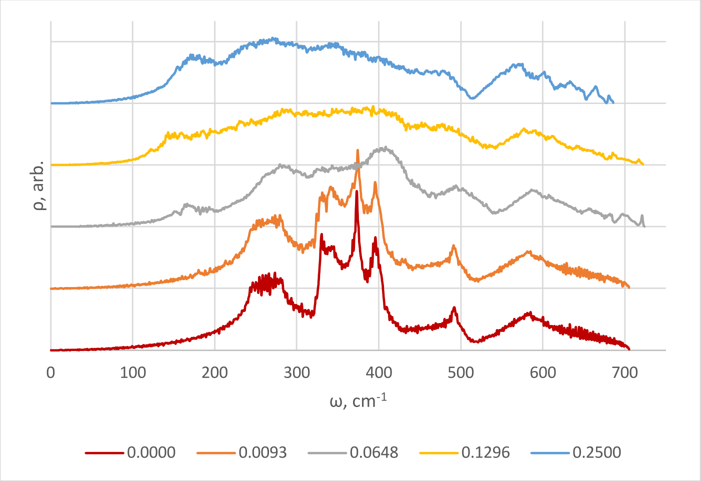

Fig. 5. Phonon DOS for cubic $Mg_{1-x}Zn_xO$ at different Zn concentrations.

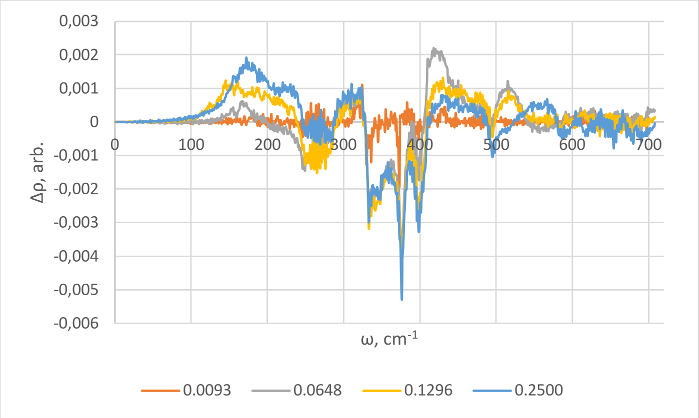

Fig. 6. Phonon DOS differences between the different cubic solid solutions and pure MgO.

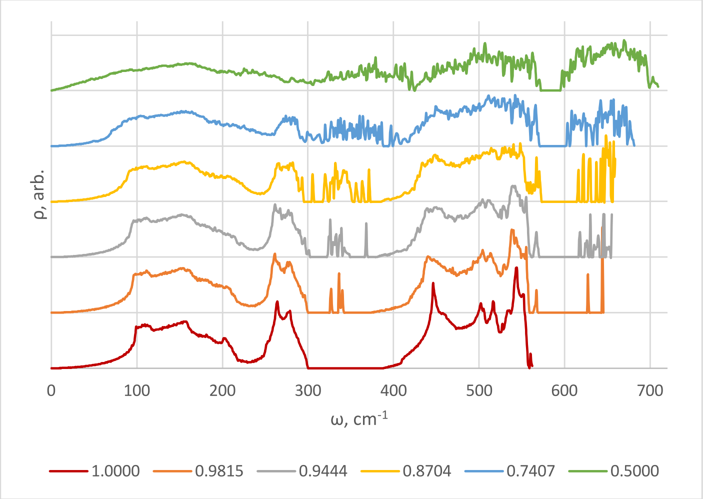

Fig. 7. Phonon DOS for wurtzite $Mg_{1-x}Zn_xO$ at different Zn concentrations.

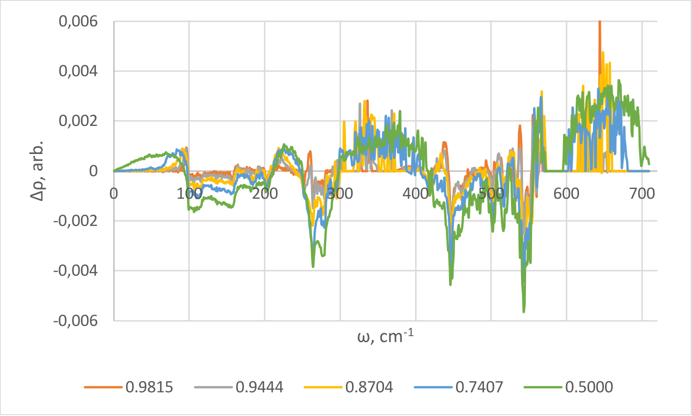

Fig. 8. Phonon DOS differences between the different wurtzite solid solutions and pure ZnO.

The figures above show the changes to the phonon DOS of $Mg_{1-x}Zn_xO$ with varying Zn content. In the case of cubic phase $Mg_{1-x}Zn_xO$ where Mg is in the majority (Figs. 5 and 6), the increase in Zn content has an effect most strongly seen as the broadening of the spectral peaks. The main MgO peaks at around 350 cm^{-1} become broad and merge with each other. This is because of the increase in disorder of the crystal, which lowers the symmetry and makes previously degenerated phonon modes distinguishable. There are no distinct local vibrational modes of Zn and O, but new vibrational frequencies do start to appear in the low frequency region at around 150 cm^{-1}, as well as around 420 cm^{-1}. There is as well an overall shift toward lower frequencies, which is due to the larger mass of the Zn atom.

In the wurtzite phase of $Mg_{1-x}Zn_xO$ where Zn is in the majority (Figs. 7 and 8), an increase in Mg content has a different effect on the DOS than in the previous case. There is not so much a spectral broadening but there are very distinct local vibrational modes of Mg and O appearing in the phonon band gaps of ZnO (300–400 cm^{-1} & above 550 cm^{-1}). There are the characteristic modes at ~350 cm^{-1} and also at high frequencies above 620 cm^{-1}. Only at high concentrations of Mg do the DOS peaks for ZnO start to broaden. The Mg and O local mode frequencies appearing in the high region, however, show that the interaction between Mg and O is stronger than between Zn and O. This together with the lower mass of the Mg atom explains the overall DOS shift toward higher frequencies.

4. CONCLUSIONS

The phonon DOS peaks for $Mg_{1-x}Zn_xO$ in the cubic phase become broader with increasing Zn content and the DOS curve in general tends toward lower frequencies. The phonon DOS peaks for $Mg_{1-x}Zn_xO$ in the wurtzite phase show less broadening; however, there are distinct local modes appearing with increasing Mg content and generally the DOS tends toward higher frequencies. The interaction Mg-O is stronger than the interaction Zn-O. Classical MD in conjunction with *ab initio* calculations is a powerful method for lattice dynamics calculations, especially when researching and modelling material defects and solid solutions where large structures are of interest.

Interatomic potentials can be found such that they describe lattice dynamics to a good degree of accuracy. New interatomic potentials have been found for the Mg-O, Zn-O, O-O interactions.

ACKNOWLEDGEMENTS

The financial support of M-ERA. NET project "ZnMgO Materials with Tunable Band Gap for Solar-Blind UV Sensors"(ZMOMUVS) is greatly acknowledged. The Institute of Solid State Physics at the University of Latvia, as the Centre of Excellence, has received funding from the European Union's Horizon 2020 Framework Program H2020-WIDESPREAD-01-2016-2017-TeamingPhase2 under Grant Agreement No. 739508, project CAMART2.

REFERENCES

1. Rohskopf, A., Seyf, H.R., Gordiz, K., Tadano, T., & Henry, A. (2017). Empirical Interatomic Potentials Optimized for Phon Properties. *Computational Materials, 3*, 1–7.
2. Choopun, S., Vispute, R.D., Yang, W., Sharma, R.P., Venkatesan, T., & Shen, H. (2002). Realization of Band Gap above 5.0 eV in Metastable Cubic-Phase MgxZn1-xO Allow Films. *Appl. Phys. Lett., 80*, 1529.
3. Hu, Y., Cai, B., Hu, Z., & Liu, Y. (2015). The Impact of Mg Content On the Structural, Electrical and Optical Properties of MgZno Alloys: A First Principles Study. *Current Applied Physics, 15* (3), 423–428.
4. Maznichenko, I., Ernst, A., Bouhassoune, M., & Henk, J. (2009). Structural Phase Transitions and Fundamental Band Gaps of MgxZn1-xO Alloys from First Principles. *Physical Review B, 80*, 144101.
5. Schleife, A., Eisenacher, M., Rödl, C., Fuchs, F., Furthmüller, J., & Bechstedt, F. (2010). Ab Initio Description of Heterostructural Alloys: Thermodynamic and Structural Properties of MgxZn1-xO and CdxZn1-xO. *Phys. Rev. B, 81*, 245210.
6. Yang, J.-L., Liu, K.-W., & Shen, D.-Z. (2017). Recent Progress of ZnMgO Ultraviolet Detector. *Chin. Phys. B*, *26* (4), 047308.
7. Jain, A., Ong, S.P., Hautier, G., Chen, W., Richards, W.D., Dacek, S., … & Persson, K.A. (2013). The Materials Project: A Materials Genome Approach to Accelerating Materials Innovation. *APL Materials*, *1*, 011002.
8. Hahn, T. (2016). *International Tables for Crystallography.* Volume A. Springer.
9. Tian, F., Duan, D., Li, D., Chen, C., Sha, X., Zhao, Z., … & Cui, T. (2014). Miscibility and Ordered Structures of MgO-ZnO Alloys under High Pressure. *Sci. Rep., 4*, 5759.
10. LAAMPS Tube. (n.d.). *Buckingham Potential*. Available at http://lammpstube.com/2020/02/10/buckingham-potential/
11. *Chapters 8 & 9 on Potential Functions*. Available at http://www.courses.physics.helsinki.fi/fys/moldyn/lectures/L4.pdf
12. CRYSTAL. (n.d.). *Crystal17*. Available at https://www.crystal.unito.it/index.php
13. Dovesi, R., Erba, A., Orlando, R., Zicovich-Wilson, C., Covalleri, B., Maschio, L., … & Kirtman, B.. (2018). Quantum-Mechanical Condensed Matter Simulations with CRYSTAL. *Wiley Interdisciplinary Reviews: Computational Molecular Science*, *8* (39). doi :10.1002/wcms.1360.
14. Curtin University. (n.d.). *GULP*. Available at http://gulp.curtin.edu.au/gulp/
15. Gale, J.D. (1997). GULP – A Computer Program for the Symmetry Adapted Simulation of Solids. *JCS Faraday Trans.*, *93*, 629.

16. CRYSTAL. (n.d.). *CRYSTAL Basis Sets*. Available at https://www.crystal.unito.it/basis-sets.php
17. Lewis, G.V., & Catlow, C.R.A. (1985). Potential Models for Ionic Oxides. *Journal of Physics C: Solid State Physics, 18* (6), 1149–1161.
18. Binks, D.J. (1994). *Computational Modelling of Zinc Oxide and Related Oxide Ceramics*. Doctoral Thesis. University of Surrey, Surrey.
19. Al-Qasir, I., Jisrawi, N., Gillette, V., & Qteish. A.H. (2015). Thermal Neutron Scattering Cross Sections of Beryllium and Magnesium Oxides. *Annals of Nuclear Energy, 87*, 242. doi:10.1016/j.anucene.2015.09.006
20. Mankad, V., Gupta, S.K., & Jha, P.K. (2016). Thermodynamic Properties of Zinc Oxide [001] Nanowires via First Principles Calculations. *Adv. Mater. Lett.,7* (3), 100. doi: 10.5185/amlett.2016.6147

LATVIAN JOURNAL OF PHYSICS
AND TECHNICAL SCIENCES
2022, N 2

DOI: 10.2478/lpts-2022-0008

MAXIMUM SHANNON INFORMATION DELIVERED IN A LECTURE

L. Alksne*, A. Ozols**

[1]Liepaja University, 14 Liela Str., Liepaja, LV-3401, LATVIA
[2] Faculty of Electronics and Telecommunications,
Riga Technical University, 12 Azenes Str., Riga, LV-1007, LATVIA
*e-mail: linda.alksne@liepu.lv
**e-mail:andris.ozols@rtu.lv

The aim of our paper is to evaluate the maximum Shannon (syntactic) information carried through a video lecture. To achieve the aim, we have considered a natural lecture delivered by a lecturer as a signal transmitted over the physical communication channel consisting of a sound sub-channel and light sub-channel. Receivers are eyes and ears of listeners whose physical characteristics are taken into account. The physiological, neurological and cognitive aspects of the problem are neglected in calculations. The method has been developed to calculate the absolute maximum values of Shannon information characteristics of a natural lecture basing on the capacity formula of continuous communication channel and physical considerations taken into account for the first time, to our knowledge. Maximum Shannon information characteristics (entropies of sound and light frames, amounts of total acoustical and optical information, capacities of sound and light sub-channels, total amount of information and total capacity) of a natural lecture perceived by the audience have been calculated. These values are the upper bounds of a video lecture. The obtained results are discussed in the paper. After some modification, the proposed method can be practically applied for the optimization of both natural and video lectures because there is some correlation between syntactic and semantic information characteristics.

Keywords: *Channel capacity, communication channel, entropy, lecture, semantic information, syntactic information, video lecture.*

1. INTRODUCTION

Conceptually, information can be thought of as being stored in or transmitted as variables that can take on different values. Informally, we obtain information from a variable by looking at its value, just as we receive information from an email by reading its contents. In the case of the variable, the information is about the process behind the variable [1]. Generally, there are two kinds of information, which are important with respect to a lecture. Shannon information provides the so-called syntactic information, which reflects the amount of statistical correlation between systems. By contrast, semantic information refers to information, which is in some sense meaningful for a system, rather than merely statistical [2]. The aim of the paper is to calculate the maximum syntactic Shannon information delivered in a video lecture. To achieve the aim, the delivery process of a natural lecture is considered from the physical point of view. Further in the paper, we always mean the Shannon information and the quantities related to it, if not mentioned otherwise.

Shannon entropy of the message ensemble X consisting of messages x_i is the average amount of information $I(x_i)$ contained in a message:

$$H(X) = \sum_{i=1}^{n} p(x_i)\, I(x_i) = \sum_{i=1}^{n} p(x_i) \log_b \frac{1}{p(x_i)} = -\sum_{i=1}^{n} p(x_i) \log_b p(x_i). \qquad (1)$$

It depends only on the statistic nature of the message source expressed by message probabilities $p(x_i)$. Here b=2 corresponds to the binary logarithm, and n is the number of messages [3].

Different applications of Shannon entropy are used to evaluate the information content of videos. As a rule, this entropy (or quantities related to it, such as mutual information, joint entropy, conditional entropy) is calculated by computer programs (e.g., [4]) within each 2D video frame based on intensity and colour of frame elements. However, entropy there is in relative units and serves to evaluate the changes. Analogously, the speech entropy is calculated and used [5].

Based on the differences between video frames, the entropy is able to serve as a measure of the complexity of changes. Due to content dependency, however, the relative entropy changes in the sequence of video frames, being a better indicator for detection [6].

Experimental video results of Xuguang Zhang [7] have shown that the panic crowd motion state has higher entropy, and the normal crowd state has lower entropy. When a panic behaviour of a crowd occurs, the pedestrians often move hurry-scurry. As the pedestrians are moving, the attributes (such as gender and age) of pedestrians are different. The speeds of the movements of individuals are also different. The motion information of the body parts (arms, torso and legs) of an individual is also different. The motion flow of the crowd video represents a state of disorder. In 2016, Luo also proposed a detection algorithm based on skeleton entropy by using the information from RGBD videos [8]. The entropy is analysed in terms of the angles of the body skeleton to find whether the values of the information entropy are significantly higher in abnormal videos than in normal videos in order to detect the most abnormal behaviours, such as fight, robbery and chaos. The principle of the highest frame entropy changes is used in video advertising [9]. The joint entropy changes and conditional entropy changes of x and y coordinates are used for the classification of landscapes [10]. Černekova et al. have demonstrated that mutual entropy and joint entropy between the frames can be used to detect cuts and extract key frames [11].

There are also other applications of Shannon entropy, for example, in video compression [12] and security [13]. An important achievement is Memorability-Entropy-based video summarization. Authors predict the memorability score by using the fine-tuned deep network and calculate the entropy value of the images. The frame with the maximum memorability score and entropy value in each shot is selected to constitute the video summary. Memorability is the quality of being worth remembering [14].

However, the authors are mostly interested in entropy and related information characteristics to improve the efficiency of video lectures. Thus, entropy can be calculated for random time slot of a random video lecture captured in classroom and for the same length of video lecture followed by a set of rules on how to produce a good video lecture [15]. These rules have already given some results while transmitting information to people. Prior studies have investigated the effect of instructional video on learning outcomes [16]. Thus, it is empirically shown that there is some correlation between Shannon entropy of videos and the efficiency of video lecture, i.e., the semantic information content.

For further development, it would be important to have not only relative information characteristics of videos, but also absolute ones. As far as we know, there are no papers dealing with the absolute Shannon information carried by lectures or by natural scenes. Therefore, the method of expert evaluations of the quality of lectures is used [17]. Basing on Shannon's communication theory (see Section 2), we propose a method how to calculate Shannon information delivered in a natural lecture using only physical properties of human sensors (eyes and ears) and neglecting any physiological processes in the brain, which are too complicated to be taken into account in this first calculation attempt. We quantitatively evaluate the maximum Shannon (syntactic) information, which can be physically delivered in a lecture of a certain length and perceived by the audience. As mentioned above, syntactic information refers only to the quantity of unexpected data not to their meaning. We suppose that a lecturer speaks and shows slides and demonstrations for a certain period of time. Thus, the audience receives a certain amount of optical and acoustical information by means of eyes and ears. This is the maximum possible information. If the lecture is captured by the video with sound and later reproduced, the information delivered in this video lecture will be reduced because of technical limitations of video recorder (limited optical and acoustical bandwidths, etc.).

In this article, natural lecture delivered by a lecturer is treated as a noiseless communication channel consisting of a sound sub-channel and light sub-channel. Maximum transmitted total amount of information in both sub-channels and in the whole channel is calculated as well as the corresponding channel capacities. Further mathematical and experimental development of the presented approach can be applied for the optimization of both natural and video lectures.

2. METHOD

The idea to calculate the Shannon information of a lecture is based on the capacity formula of continuous communication channel:

$$C_{sample} = \max I(X,Y) \text{ bits/sample,} \quad (2)$$

where $I(X,Y)$ is an averaged mutual information of ensemble of received signals Y with respect to ensemble of transmitted signals X per sample[3, p.586]. If the channel has a fixed bandwidth B, then the maximum signalling rate is Nyquist rate $2B$ according to the sampling theorem, and channel capacity is as follows:

$$C = 2B \max I(X,Y), \text{ bits/s.} \quad (3)$$

Transmission of a lecture to the audience can be regarded as a communication channel consisting of a sound sub-channel and a light sub-channel. They have different known frequency bandwidths determining the maximum signalling rates. The main problem is to determine the mutual information of sound sub-channel and light sub-channel. However, we can avoid this problem neglecting the noise. In this case, mutual information in each sub-channel can be replaced by its Shannon entropy $H(X)$ [3]. However, for continuous signals the probabilities of their values x $p(x)=w(x)dx$ in Eq. (1) become infinitesimally small (here $w(x)$ is the differential probability distribution function). To overcome this problem we assume that we can approximately replace infinitesimally small probabilities $p(x)=w(x)dx$ by small but finite probabilities $p(x)=w(x)\Delta x$, which can be numerated. Shannon entropies can be calculated by appropriate quantization of different parameters x coding the transmitted information (e.g., sound and light intensity or frequency) in intervals Δx. In this article, we are interested in the maximum Shannon information; therefore, quantization intervals are determined based on the human resolving power of coding parameters. Thus, based on this hypothesis, we can calculate not only the maximum Shannon entropies of sound and light channels but also maximum capacities of these channels and transmitted information during the lecture.

Further we shall explain our method in more detail using as an example the woman lecturer who delivers a lecture, the duration of which is ten minutes (t = 10 min).

3. DETAILED EXPLANATION OF THE METHOD RESULTS

At first, we consider sound and light sub-channels separately.

3.1. Entropy of the Sound Channel

We assume that the lecturer is a woman whose voice is soprano. Her speech is characterised by sound intensity, I_s, sound intensity modulation frequency bandwidth, $F_{s\ \mathrm{mod}}$, and by sound frequency, f_s. Fundamental frequencies of soprano belong to the spectral interval f_s = 260–1050 Hz [18]. They bring the main sound energy of the speaker. In the case of soprano singer harmonics up to the fourth can also play a significant role [19]; however, our woman is a lecturer, not a singer. Thus, we assume that her sound frequency bandwidth is F_s = 790 Hz. Humans can perceive sound intensity changes with the modulation bandwidth of about $F_{s\ mod}$ = 500 Hz [20]. This means that we can hear faster than we see because the corresponding light intensity modulation bandwidth for humans is only about 10 Hz (see Section 3.3). It should be stressed that both intensity bandwidths refer to the envelope function of intensity time dependence.

Due to the limited sound intensity modulation bandwidth, the sound signal can be sampled with the sampling time interval [3]:

$$\Delta t_s = \frac{1}{2 \times F_{s\ mod}} = 1 \times 10^{-3} s ,$$

and we can consider only sampled moments instead of the continous time. At each sampled time moment, the listeners perceive the sound frame – the sound spectrum $I_s(f_s)$, which carries the spectral sound information at the given moment (this is necessary because only the envelope of sound intensity time dependence is taken into account for sampling). In principle, there is an infinite number of possible sound frames at the certain sampled moment of time because sound intensity and frequency vary continously. As mentioned above in Section 2, we have to make these variables discrete. On the other hand, this quantization occurs naturally because the human ear has limited intensity and frequency resolution power. Thus, a sound frame is a 2D message from the point of view of communication theory. The lecturer is a source of these messages, which follow at frequency $2F_{s\ mod}$. The average information per such a message by definition equals the Shannon entropy of the ensemble of all such messages according to Eq. (1).

Thus, the calculation of the Shannon entropy is based on the making discrete the sound frame variables, I_s and f_s, taking into account the resolution power of human ear. We divide the sound frequency in intervals Δf_s =1 Hz [the minimum frequency difference which can be resolved by ear [21]] and sound intensity intervals $\Delta I_s = 1.2 \times 10^{-6}$ W/m^2 corresponding to the minimum noticable sound pressure changes of 0.5 dB [22]. Thus, there are

$$\frac{F_s}{\Delta f_s} = \frac{790}{1} = 790$$

discrete sound frequency intervals. If we assume that the highest sound intensity of the speaker corresponds to fortissimo (100 dB or 10^{-2} W/m^2), then (keeping only integers because fractional sound intensity interval cannot be resolved by a human ear) we have

$$\frac{I_{s\max}}{\Delta I_s} = \frac{10^{-2}}{1.2 \times 10^{-6}} \approx 8333$$

sound intensity intervals which can be resolved by the ear. In this way, we can divide the sound frame into $N_s = 790 \times 8333 =$ 6583070 2D ($\Delta I_s \times \Delta f_s$) cells.

Depending on the sound signal, each cell can be either filled or empty. For simplicity we assume that the fulfilment probabilities are equal for all cells. Sound frames differ by the number and distribution of filled and empty cells. As mentioned above, each frame can be regarded as a message. To get the maximum frame entropy the probabilities of these messages should be equal [3]. This can be readily seen from the Shannon entropy expression (1) letting all the probabilities of n messages to be equal:

$$p(x_i) = 1/n , \qquad (4)$$

$$H(X) = \log_2 n. \qquad (5)$$

How many messages are there? For the fixed number of filled cells, k, there are ${C_{N_s}}^k$ messages, where ${C_{N_s}}^k$ is the number of combinations for fixed k of a set of N_s elements. Number k can vary from 0 to N_s. Therefore, we have to sum all ${C_{N_s}}^k$ for $k = 0, 1,2,..... N_s$ and to obtain the number of combinations for all k. The result is [23]:

$$\sum_{k=0}^{N_s} C_{N_s}^k = 2^{N_s}. \qquad (6)$$

Thus, the number of messages is $n = 2^{Ns}$ and the maximum entropy of the sound frame is [3]:

$$H_{s\,max} = \log_2 2^{Ns} = N_s. \qquad (7)$$

Previously, we have found that $N_s = 6583070$; therefore, $H_{s\,max} = 6583070$ bits.

3.2. Total Maximum Information in the Sound Sub-channel and its Capacity

Let us find the total maximum information transmitted over the sound sub-channel. During the lecture of duration $t = 600$s, the number of transmitted sound frames is:

$$\frac{t}{\Delta t_s} = \frac{600}{1\times10^{-3}} = 600000 \quad .$$

Each sound frame carries the maximum average information $H_{s\ max} = 6583070$ bits as shown in the previous section. Assuming that all messages (sound frames) are statistically independent, we find that the total maximum transmitted information over the sound sub-channel is [3]:

$$Info_{s\,max} = \left[\frac{t}{\Delta t_s}\right] \times H_{s\,max}. \qquad (8)$$

Putting all the known quantities t=600s, $\Delta t_s = 1.0\times10^{-3}$ s and $H_{s\ max} = 6583070$ bits in Eq.(8) yields $Info_{s\ max} = 3.95\times10^{12}$ bits. Here and further we keep the number of digits to have accuracy not worse than 0.3 %.

The communication channel capacity is defined as the maximum amount of information transferred per second [3]. Thus, the maximum capacity of our noiseless sound sub-channel is:

$$C_{s\,max} = \frac{Info_{s\,max}}{t} = \frac{H_{s\,max}}{\Delta t_s}. \qquad (9)$$

Putting the above-mentioned values of $Info_{s\,max}$ and t, or of $H_{s\,max}$ and It_s in Eq. (9), we get $C_{s\,max} = 6.58\times10^9$ bits/s.

3.3. Entropy of the Light Frame

We consider the optical information transmission in light sub-channel analogously to that of sound sub-channel. Light sub-channel is characterized by the light intensity $I_{l,}$, light intensity modulation frequency bandwidth $F_{l\,mod}$ describing the speed of the light intensity temporal changes, light frequency f_l determining the image colours (we neglect the eye sensitivity spectral dependence), field of view angles along the transversal coordinates of the scene x and y, θ_x and θ_y, and the transmission time t, which is the same as for the sound sub-channel.

The maximum light frame (image) rate is determined by the light intensity modulation bandwidth of eye, $F_{l\,mod,}$ which is equal to 10 Hz at the eye contrast sensitivity function level of 200. This level corresponds to the light intensity resolution of 0.5 % by the human eye. Smaller intensity differences cannot be resolved [24]. This means that there are

$$\frac{I_{l\max}}{\Delta I_l}=\frac{1}{0.005}=200$$

discrete detectable light intensity intervals. On the other hand, according to the sampling theorem, light intensity envelope time dependence can be sampled with the sampling time interval

$$\Delta t_i=\frac{1}{2\times F_{l\max}}=\frac{1}{2\times 10Hz}=5\times 10^{-2}s\,.$$

For fixed sampling time, the audience perceives optical image, the light frame, determined by the light intensity I_l dependence on f_l, θ_x and θ_y. This image is a 4D message from the point of view of Shannon's information theory. Again, the average information per such a message by definition equals to the Shannon entropy of the ensemble of all such messages, as shown in Eq. (1).

Further, light frame entropy calculation is analogous to the sound frame entropy calculation described in Section 3.1. We divide the light frequency into intervals $\Delta f_l = 3.0\times 10^{12}$ Hz. This is the minimum frequency difference which can be resolved by eye [25]. The visible spectral range in video lecture we assume to be from 400 to 750 nm [26] which corresponds to the light frequency range $F_l = 3.5\times 10^{14}$ Hz. Thus, there are (keeping again only integers)

$$\frac{F_l}{\Delta f_l}=\frac{3.5\times 10^{14}}{3.0\times 10^{12}}=116$$

resolvable light frequency intervals. [Here we would like to stress that the number of colours perceived by a human is much larger. Human brain constructs colours from the perceived frequencies of different intensities within these intervals. We are restricting ourselves only to physical rather than physiological processes involved in the delivery of lecture.]

The minimum intervals of viewing angles, θ_x and θ_y, are determined by the accepted minimum detectable light intensity changes of 0.5% and are equal to $\Delta\theta$=15 arc minutes=4.36×10^{-3} rad [24]. The maximum horizontal eye field of view along the horizontal x-axes is $\theta_{x\ max} = 160^0 = 2.79$ rad and along the vertical one $\theta_{ymax} = 130^0 = 2.27$ rad [18], [27]. Therefore, there are

$$\frac{\theta_{x\max}}{\Delta\theta}=\frac{2.79}{4.36\times 10^{-3}}=640$$

and

$$\frac{\theta_{\mathrm{y}\max}}{\Delta\theta}=\frac{2.27}{4.36\times 10^{-3}}=520$$

intervals along the θ_x and θ_y axes, respectively (analogously as in the sound channel, fractional angular intervals cannot be resolved by a human eye).

There are N_l 4D cells in one light frame, where

$$N_i=\frac{I_{l\max}}{\Delta I_l}\times\frac{F_l}{\Delta f_i}\times\frac{\theta_{x\max}}{\Delta\theta}\times\frac{\theta_{y\max}}{\Delta\theta}=7720960000\approx 7.72\times 10^9\,.$$

We can directly apply Eqs. (6) and (7) to the light sub-channel replacing the number of 2D cells N_s by the number of 4D cells N_l, because the result depends only on the number of cells but not on their dimensionality. Thus,

$$H_{l\ max}=\log_2 2^{N_l}=N_l \tag{10}$$

and $H_{l\ max} = 7.72\times 10^9$ bits.

3.4. Total Maximum Information in the Light Sub-channel and its Capacity

Total maximum information in the light sub-channel and its corresponding capacity are calculated in the same way as in the case of sound sub-channel (Section 3.2). Therefore,

$$Info_{l\,max} = \left[\frac{t}{\Delta t}\right] \times H_{l\,max} \tag{11}$$

and

$$Info_{l\max} = \frac{600}{5\times10^{-2}} \times 7.72\times10^{9} \approx 9.26\times10^{13}\,bits\,.$$

Instead of (8) in the light sub-channel we have

$$C_{l\,max} = \frac{Info_{l\,max}}{t} = \frac{H_{l\,max}}{\Delta t_l} \tag{12}$$

and, consequently, putting the values $Info_{l\,max}$ and t, or $H_{l\,max}$ and Δt_l in Eq.(10) we get $C_{l\,max} \approx 1.54\times10^{11}$ bit/s.

3.5. Total Maximum Information of the Lecture and the Capacity of the Lecture as a Communication Channel

The obtained information characteristics of sound and light sub-channels enable one to find the maximum information and maximum capacity of the whole lecture by simply summing the corresponding quantities because we can assume them to be independent. In this way, the maximum information delivered by the considered lecture is as follows:

$$Info_{max} = Info_{s\,max} + Info_{l\,max}, \tag{13}$$

and the maximum capacity of the whole lecture channel is as follows:

$$C_{max} = C_{s\,max} + C_{l\,max}, \tag{14}$$

because amounts of information can be always summed, and the information transmittance time is the same for both sub-channels. Putting the corresponding quantities in Eqs. (13) and (14) we get $Info_{max} = (3.95\times10^{12} + 9.26\times10^{13})$ bits $\approx 9.65\times10^{13}$ bits, and $C_{max} = (6.58\times10^{9} + 1.54\times10^{11})$ bits/s $\approx 1.61\times10^{11}$ bits/s.

4. DISCUSSION

It is clearly seen from results of the previous section that Shannon (syntactic) information characteristics of the whole lecture channel are almost completely determined by the light sub-channel because information carried by the sound sub-channel is lower by more than one order of magnitude. The ratio of entropies of light and sound frames is even higher:

$$\frac{H_{l\max}}{H_{s\max}} = \frac{7.72\times10^{9}}{6583070} \approx 1173\,.$$

Thus, the contribution of the lecturer's voice to the syntactic information is almost negligible. At the first glance, this result seems to be expected because vision ranks highest in the hierarchy of human senses. In the lecture, it seems that only the demonstration of slides is necessary. On the other hand, this is a paradoxical result because practically we know that the role of the lecturer is of primary importance. This paradoxical result is the consequence of neglecting the meaning of the lecture when calculating the syntactic Shannon information. Not only the voice but also the intonation and gestures of the lecturer play an important role expressing the attitude of the lecturer to the content. It should be also noted that if the lecturer used additional sound accompaniment, e.g., music, with larger sound frequency bandwidth up to 20 kHz (the maximum bandwidth of a human ear [18]), then $H_{s\ max}$, $Info_{s\ max}$ and $C_{s\ max}$ would increase by more than one order of magnitude achieving their maximum possible values comparable to the corresponding light sub-channel parameters. This situation takes place in concerts.

We can compare the above calculated capacities of sound and light sub-channels with the known information capacities of the human hearing and human sight. We have found that $C_{s\ max} = 6.58\text{x}10^9$ bits/s and $C_{l\ max} = 1.54\text{x}10^{11}$ bits/s whereas the capacity of human hearing channel is about 10^4 bits/s and human sight channel is about 10^7 bit/s, respectively, as evaluated by Temnikov et al. [28]. More recent results for these human sensor channels are similar – about 10^5 bit/s and about 10^7 bits/s [29]. Our calculated capacity values are larger by 4–5 orders of magnitude.

How such a large difference can be explained? First of all, we have calculated the maximum capacity values of a natural lecture, which serve as upper bounds of sound and light sub-channels. This implied that all cells and all frames were equally probable. Practically this is not the case because the sensitivity of ears and eyes are spectrally selective. For example, the human ear is the most sensitive to the sounds in the frequency range from 1500 to 4000 Hz, but the human eye is the most sensitive at the green–yellow light wavelength of 555 nm ($5.4\text{x}10^{14}$ Hz) [18]. Also, the content of a lecture can influence the frame probabilities. In our calculations, we have also neglected the presence of noise in both sound and light sub-channels. Finally, the perceived light and sound information transmission in a nervous system and its processing in the brain are neglected. It is known that a huge information compression takes place there [29]. Evidently, optical and acoustical perception systems of humans are not able to perceive all the physically available information.

Thus, the obtained results for a natural lecture are overestimated. Yet, they can be used as upper limits for corresponding quantities of a video lecture because the information characteristics will be much lower due to the technical limitations of the video camera.

The proposed calculation method of Shannon information characteristics can be used not only to find their maximum values but also, in more general case, to introduce the probability distributions of cells in all frames and also to vary the cell size. The appropriate variations of probability distributions and cell sizes would enable one to meet the empirical conditions [15] of an optimal lecture. Thus, information characteristics of an optimal lecture could be calculated. It should be noted that the mathematical modification of the presented approach is needed in this case.

The method based on the capacity formula (3) of continuous communication channel we have proposed in Section 2 and used to calculate the maximum Shannon information characteristics of a natural lecture is not precise. However, we believe that the method is logical and the made approximations do not dramatically change the results. To prove its practical applicability, further theoretical and experimental studies are necessary.

In principle, the proposed method is quite general. It can be also applied for the calculation of syntactic optical and acoustical information characteristics of any object in the world, e.g., landscapes and streets with people, cosmic objects, etc.

5. CONCLUSIONS

1. The method has been developed to calculate the absolute maximum values of Shannon information characteristics of a natural lecture based on the capacity formula of continuous communication channel and physical considerations taken into account for the first time, to our knowledge. After some modification, it can be practically applied for the optimization of both natural and video lectures because there is some correlation between syntactic and semantic information characteristics.
2. Maximum Shannon information characteristics (entropies of sound and light frames, amounts of total acoustical and optical information, capacities of sound and light sub-channels, total amount of information and total capacity) of a natural lecture perceived by the audience have been calculated. These values are the upper bounds of a video lecture.
3. It has been found that physically the maximum capacity of sound sub-channel $C_{s\ max} = 6.58\times10^9$ bits/s is almost negligible compared to the maximum capacity of light sub-channel $C_{l\ max} = 1.54\times10^{11}$ bits/s. It is the consequence of neglecting meaning in the syntactic information.
4. Capacities of sound and light sub-channels are by 4–5 orders of magnitude larger than the previously estimated capacities of human hearing and vision information channels because of the used approximations and due to neglecting the physiological processes of the information transmission in nervous system and its processing in the brain.
5. Further theoretical and experimental work is needed to develop and prove the proposed method.

REFERENCES

1. Vajapeyam, S. (2014). *Understanding Shannon's Entropy Metric for Information*. eprint arXiv:1405.2061
2. Kolchinsky, A., & Wolpert, D.H. (2018). Semantic Information, Autonomous Agency and Non-equilibrium Statistical Physics. *Interface Focus, 8*, 20180041. http://dx.doi.org/10.1098/rsfs.2018.0041.
3. Carlson, Bruce A. (1986). *Communication Systems. An Introduction to Signals and Noise in Electric Communication.* New York: McGraw-Hill Book Company.
4. MathWorks. (n.d.). *Entropy.* Available at https://se.mathworks.com/help/images/ref/entropy.html
5. MathWorks. (n.d.). *Signal.* Available at https://www.mathworks.com/helps/signal/ref/pentropy.html#mw_da069ed5-a376-4d11-84d3-ca16946eab9
6. Seeling, P. (2010). Scene Change Detection for Uncompressed Video. *Technological Developments in Education and Automation*. doi:https://doi-org.resursi.rtu.lv/10.1007/978-90-481-3656-8_3
7. Xuguang Zhang, X. S. (2019). Crowd Panic State Detection Using Entropy of the Distribution. *Physica A: Statistical Mechanics and its Applications, 525* (7), 935–945. doi: 10.1016/j.physa.2019.04.033
8. Luo, Z. B. (2016). Human Abnormal Behavior Detection Based on RGBD Video's Skeleton Information Entropy. *Lecture Notes in Electrical Engineering.* doi:https://doi-org.resursi.rtu.lv/10.1007/978-3-662-49831-6_74

9. Ferreira, T.A.F.R (2014). *Entropy Based Dynamic Ad Placement Algorithms in Video Advertising*. PhD Thesis, University of Beira Interior, Covilha, Portugal.
10. Nowosad, J. & Stepinski, T.F. (2019). Information Theory as a Consistent Framework for Quantification and Classification of Landscape Patterns. *Landscape Ecol., 34*, 2091–2101.
11. Černekova, Z., Nikou, C., & Pitas, I. (2002). Entropy Metrics used for Video Summarization. *Proceedings of the Spring Conference on Computer Graphics*, Budmarice, Slovakia, 73–82.
12. Liu, J., Wang, Sh., Ma, Wei-Chiu, Shah, M., Hu, R., Dhawan, P. & Urtasan, R. (2020). Conditional Entropy Coding for Efficient Video Compression. *Image and Video Processing*. ECCV, LNC3, 12362, 453–468. https://doi.org/10.1007/978-3-030-58520-4_27.
13. Sun, J., Xu, Zh., Liu, J., & Yeo, Y. (2011). An Objective Visual Security Assesment for Cipher-Images Based on Local Entropy. *Multimed. Tools Appl., 53*, 75–95.
14. Fei, M., Jiang, W., & Mao, W. (2017). Memorable and Rich Video Summarization. *J. Vis. Comun. Image Represent. 42* (C), 207–217.
15. Alksne, L. (2016). How to produce video lectures to engage students and deliver the maximum amount of information. *Proceedings of the International Scientific Conference "Society. Integration. Education",* 503–516. doi: http://dx.doi.org/10.17770/sie2016vol2.1424
16. Wieling, M., & Adriaan Hofman, W.H. A. (2010). The Impact of Online Video Lecture Recordings and Automated Feedback on Student Performance. Computers & Education, 54 (4), :992-–998. doi: 10.1016/j.compedu.2009.10.002
17. Pauliks, R. (2016). *Quality Studies of Video Transmission Services in Packet Networks*. Summary of PhD Thesis. Riga: RTU Publishing House. (in Latvian).
18. Jehonovičs, A. (1984). *Handbook of Physics and Technics*. Rīga: Zvaigzne. (in Latvian).
19. Smith, J. (2007). *Why Can an Opera Singer be Heard over the Much Louder Orchestra?* Available at https://www.scientificamerican.com/article/expert-opera-singer/
20. Horowitz, S. (2013). *The Universal Sense: How Hearing Shapes the Mind.* USA: Bloomsbury.
21. Nave, C.R. (2016). *Hyperphysics.* Atlanta: Georgia State University.
22. Errede, S. (2002–2017). The Human Ear-Hearing, Sound Intensity and Loudness Levels. *UIUC Physics 406 Acoustical Physics of Music*,1–33.
23. Benjamin, A.T., & Quinn, J.J. (2003). *The Proofs that Really Count. The Art of Combinatorial Proof.* The Dolciani Mathematical Expositions 27, The Mathematical Association of America, ISBN 978-0-88385-333-7.
24. Gaisler, W.S, & Banks, M.S. (2010). Visual perfomance. In M. Bass, *Handbook of Optics, vol. III. Vision and Vision Optics* (pp. 2.1–2.51). New York: McGraw Hill Companies, Inc.
25. Luizov, A.V. (1989). Colour and Light. Leningrad: Energoatomizdat. (in Russian).
26. Richards, A. (2011). *Alien Vision. Exploring the Electromagnetic Spectrum with Imaging Technology.* (2nd ed.). Bellingham, Washington: SPIE Press.
27. Werner, J.S., Schefrin, B.E., & Bradley, A. (2010). Optics and Vision of the Aging Eye. In M.Bass*, Handbook of Optics, vol. III. Vision and Vision Optics* (pp.14.1–14.38). New York: McGraw Hill Companies, Inc.
28. Temnikov, F.E., Afonin, V.A., & Dmitriev, V.I. (1971). *Theoretical Foundations of Information Technics.* Moscow: Energija. (in Russian).
29. Markowsky, G. (2017). *Information Theory*. Encyclopaedia Britannica. Available at https://www.britannica.com/science/information-theory

sciendo

LATVIAN JOURNAL OF PHYSICS
AND TECHNICAL SCIENCES
2022, N 2

DOI: 10.2478/lpts-2022-0009

IDENTIFICATION OF THE PARAMETERS OF A THREE-PHASE ASYNCHRONOUS MOTOR FOR INTELLIGENT MONITORING SYSTEMS

V. Makarov[1], V. Zagirova[1], G.Vagapov[2], L. Grackova[3]

[1] Department of Electric Motors and Electrotechnics,
Kazan National Research Technological University,
68 Karl Marx Str., Kazan, 420015, RUSSIA
e-mail: electroprivod@list.ru
[2] Department of Methods of Increase
of Power Supply Reliability and Power Quality
in Distributive Electrical Grids,
Kazan State Power Engineering University,
51 Krasnoselskaya Str., Kazan, 420066, RUSSIA
e-mail: vagapov@mail.ru
[3] Laboratory of Energy System Analysis and Optimisation,
Institute of Physical Energetics,
14 Dzerbenes Str., Riga, LV-1006, LATVIA
e-mail: larisa.grackova@inbox.lv

The study presents an algorithm and a mathematical model for evaluating the parameters of the equivalent circuit of an asynchronous electric motor for intelligent monitoring systems. To identify the parameters of electric motors, a gradient descent method is used to find the minimum of a positive function. The algorithm and mathematical model were tested not only theoretically, but also in laboratory experiments. The results obtained proved that the proposed algorithm was an efficient and accurate method for estimating parameters. Computer modelling and experimental research confirmed the possibility of using the algorithm and the device for identifying parameters in the construction of control systems for a variable frequency drive with three-phase asynchronous electric motors in practice.

Keywords: *Generalized electric machine, gradient descent method, three-phase induction motor, variable measurement.*

1. INTRODUCTION

Nowadays, three-phase induction motors are commonly used in the national economy, since they have advantages over other types of motors. Some of the advantages of induction motors are the following: relatively simple design and operation, low cost compared to other motors and reliable operation with minimal maintenance costs. To implement the control of an induction motor operating as part of a variable frequency drive, it is necessary to know the current values of the parameters of the phase and load equivalent circuit. During operation of the induction motor, parameters can change for a number of different reasons. Therefore, in order to implement more accurate control algorithms that provide effective energy and resource saving, it is necessary to evaluate the parameters to handle variations during operation.

The main parameters that change during operation are the following: active resistances and phase inductances of the stator and rotor windings, the mutual inductance of the rotor and stator windings, the total moment of inertia of the moving parts and the static moment. Usually, a T-shaped equivalent circuit is used to analyse the operation of an asynchronous motor. The practical and theoretical studies on the field of operation of three-phase induction motors are timely and promising in all regions of the world. They reflect different approaches to solve the set goals, which are of considerable theoretical and practical importance. For example, studies have shown that changes in the active resistance of the stator winding in the intermittent periodic duty mode can be up to 30 %. At the same time, the direct start mode can change the inductance up to 40 %, and the active resistance of the rotor will increase by more than one and a half times.

All of these examples indicate that information about engine parameters during operation is very important. Unfortunately, in practice, a significant part of the electromagnetic parameters at any given time cannot be measured due to the lack of widespread implementation of stationary digital oscilloscopes with high resolution. For all these reasons, researchers are developing different theoretical approaches and methods for parameter estimation and corresponding equivalent circuits [1]–[7].

Thus, the aim of the study is an algorithm for identification of the parameters of the phase and load equivalent circuit: active resistances and phase inductances of stator and rotor windings; mutual inductance; the total moment of inertia of moving parts and static moment by applying of gradient descent method.

2. INDUCTION MOTOR DRIVE WITH IDENTIFICATION DEVICE

Asynchronous motors with a squirrel-cage rotor are most often used in the operation of drives of general industrial mechanisms, and preference is given to drives according to the “frequency converter – asynchronous motor” (FC-AM) scheme. In this case, for effective control of an induction motor (IM) operating as part of a variable frequency drive, the current values of the parameters of the phase and load equivalent circuit are mandatory information.

The main parameters of the T-shaped

equivalent circuit of the IM phase are the following: active resistances and phase inductances of the stator and rotor windings, as well as mutual inductance. Also, the total moment of inertia of the moving parts and the static moment are the most significant load parameters. It should be noted that all these values change during motor operation. For example, changes in the active resistance of the stator winding in intermittent operation can reach 30 % and the active resistance of the rotor can change more than one and a half times. In the case of using the direct start mode, the inductive reactance can vary up to 40 %. All of the above indicates that it is important to determine the current values of the parameters directly during the operation of the motor.

Unfortunately, significant part of the parameters cannot be measured directly. Therefore, in order to implement the most accurate control algorithms that provide effective energy and resource conservation, it is necessary to identify the listed parameters. On the way to creating identification methods, the following difficulties are most often found:

- Excessive requirements for the computing resources of the microcontroller;
- The computational complexity faced in real-time implementation;
- Inappropriateness of using expensive or inconvenient sensors in operation;
- The presence of contradictions between the speed, accuracy, reliability and high cost of the identification procedure (cost of equipment, payment of highly qualified personnel).

For these reasons, it is proposed to identify the parameters of an asynchronous motor on the basis of a gradient descent method for finding the minimum of definitely positive functions from the residuals of the equations of the electric motor. Gradient descent is used when the parameters cannot be calculated analytically and must be searched for by an optimization algorithm. Quantitative observation method and data collection are also used for this purpose [8], [9]. The object of the study is a three-phase squirrel-cage induction motor as part of a variable frequency drive. Measurements and data collection are carried out for the following parameters: currents and voltage of the stator phase winding, rotational speed and angular acceleration. The Generalized Theory of Electrical Machines (GEM) is used to cover a wide range of electrical machines in a unified manner [10]–[15].

Since the mathematical description of the GEM is used to identify the parameters, the control system has a coordinate converter that converts the values of a three-phase squirrel-cage induction motor into the values of the GEM and vice versa. The main measurements and data collection are declared as follows:

- $i_{1A}(t), i_{1B}(t), i_{1C}(t)$ are currents and $u_{1A}(t), u_{1B}(t), u_{1C}(t)$ are voltages of the three-phase set of stator windings;
- $\omega(t)$ is rotation frequency and $\omega(t)$ is angular acceleration of the three-phase set of rotor windings;
- R_1 and R_2 are stator and rotor phase winding resistance;
- L_1 and L_2 are stator and rotor phase winding inductance;
- M_m is mutual inductance between stator and rotor phase winding;
- J_Σ is total moment of inertia of rotating parts;
- M_c is static moment of inertia.

Figure 1 demonstrates an overall framework of the algorithm based on the induction motor drive scheme. The working principles of the proposed algorithm are as follows.

- The control object is mechanically connected to the three-phase induction motor and to the sensor block.
- The coordinate converter transforms the phase quantities of the three-phase induction motor into the electrical machine values and also calculates the derivatives of the electrical machine currents.
- On the basis of the information coming from the sensor block and the coordinate converter in the identification device, the parameters ($R_1(t)$, $L_1(t)$, $R_2(t)$, $L_2(t)$, $M_m(t)$, $J_\Sigma(t)$, $M_c(t)$) are estimated, formed and presented.
- The induction motor receives information from the frequency converter.
- The frequency converter receives a signal for setting the required electromagnetic torque $M_{\acute{y}}^{o}(t)$ and signals of parameter estimates from the identification device.
- The control device receives input data $\alpha_o(t)$, $\omega_o(t)$ and feedback data $\alpha(t)$, $\omega(t)$ from the respective sensors, as well as the parameters ($R_1(t)$, $L_1(t)$, $R_2(t)$, $L_2(t)$, $M_m(t)$, $J_\Sigma(t)$, $M_c(t)$) from the identification device. In accordance with the data received, in the control device an algorithm for frequency control of the torque and speed of the induction motor is generated.

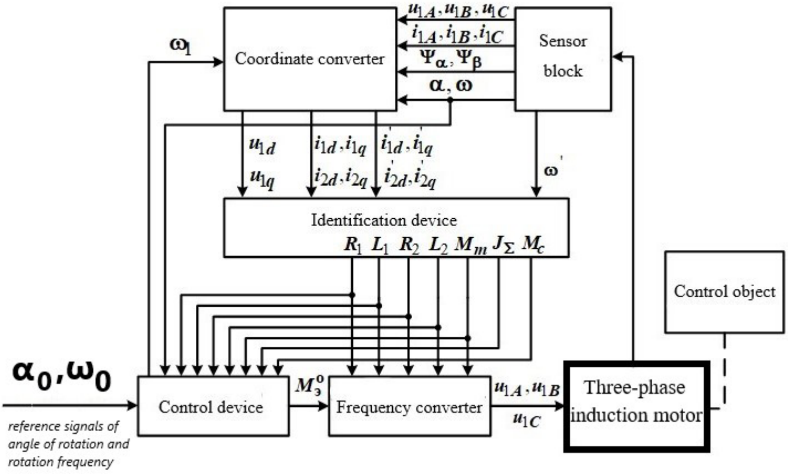

Fig. 1. The overall framework of the algorithm.

3. IDENTIFICATION OF THE PARAMETERS BY CONTINUOUS GRADIENT METHOD

Gradient descent method is an optimization algorithm that is used to find the minimum of a function, where the investigated parameters are calculated according to the mathematical model. The mathematical assessment of the load and parameters of a three-phase asynchronous motor is determined by five residual equations and seven parameters. At the same time, the missing information for the mathematical description is determined by the following test signals: phase voltage of the stator winding and angular velocity.

3.1. Mathematical Modelling

The system of GEM equations for the true values of the parameters is presented by Eq. (1):

$$\begin{cases} u_{1d} = R_{1\text{o}} i_{1d} + L_{1\text{o}} i_{1d}^{'} + M_{m\text{o}} i_{2d}^{'} - \omega_1 \left(L_{1\text{o}} i_{1q} + M_{m\text{o}} i_{2q} \right); \\ u_{1q} = R_{1\text{o}} i_{1q} + L_{1\text{o}} i_{1q}^{'} + M_{m\text{o}} i_{2q}^{'} + \omega_1 \left(L_{1\text{o}} i_{1d} + M_{m\text{o}} i_{2d} \right); \\ 0 = R_{2\text{o}} i_{2d} + L_{2\text{o}} i_{2d}^{'} + M_{m\text{o}} i_{1d}^{'} - \omega_2 \left(L_{2\text{o}} i_{2q} + M_{m\text{o}} i_{1q} \right); \\ 0 = R_{2\text{o}} i_{2q} + L_{2\text{o}} i_{2q}^{'} + M_{m\text{o}} i_{1q}^{'} + \omega_2 \left(L_{2\text{o}} i_{2d} + M_{m\text{o}} i_{1d} \right); \\ J_{\Sigma\text{o}} \omega^{'} = p_{\text{п}} \left(p_{\text{п}} M_{m\text{o}} \left(i_{2d} i_{1q} - i_{2q} i_{1d} \right) - M_{\text{co}} \right), \end{cases} \tag{1}$$

where

ω_1 – frequency of rotation of the coordinate system *d, q*;

ω_2 – slip frequency ($\omega_2 = \omega_1 - \omega$);

ω – rotor speed, el. rad/s;

$\omega^{'}$ – derivative of the rotor speed (angular acceleration);

i_{2d} , i_{2q} – currents of phases of the winding of the rotor of the GEM;

$p_{\text{ï}}$ – a number of pole pairs; indices $_{\text{o}}$ – the true values of the parameters.

Squirrel cage currents are not measured. The values of the rotor currents i_{2d} , i_{2q} are re-constructed based on the flux linkage signals Ψ_α and Ψ_β received from the Hall sensors.

At the same time, the equations of the stator flux linkage along the axes *d*, *q* are determined by Eq. (2):

$$\Psi_d = M_m \left(i_{1d} + i_{2d} \right) \text{ and } \Psi_q = M_m \left(i_{1q} + i_{2q} \right). \tag{2}$$

The conversion of stator currents i_{2d} , i_{2q} to the d-q axes is carried out in accordance with Eq. (3):

$$i_{2d} = \frac{\Psi_d}{M_m} - i_{1d} \quad \text{and} \quad i_{2q} = \frac{\Psi_q}{M_m} - i_{1q} . \tag{3}$$

Further, the estimation theory is used. Estimation theory deals with finding numerical values of parameters from a given set of data; therefore, the following values are accepted: R_1 , L_1 , R_2 , L_2 , M_m , J_Σ , M_{c} . These values are parameter estimates at any time and differ from the true values. In an ideal case, the parameters should coincide. However, they differ from the true values of the parameters. Thus, deviations arise, which are called residuals (they are also called "errors"). In the process of identifying the parameters, the residuals tend to zero, and the task of minimizing the functions is performed. The equations for calculating the discrepancies are as follows:

$$\begin{cases} \Delta u_{1d} = R_1 i_{1d} + L_1 i_{1d}^{'} + M_m i_{2d}^{'} - \omega_1 \left(L_1 i_{1q} + M_m i_{2q} \right) - u_{1d} ; \\ \Delta u_{1q} = R_1 i_{1q} + L_1 i_{1q}^{'} + M_m i_{2q}^{'} + \omega_1 \left(L_1 i_{1d} + M_m i_{2d} \right) - u_{1q} ; \\ \Delta u_{2d} = R_2 i_{2d} + L_2 i_{2d}^{'} + M_m i_{1d}^{'} - \omega_2 \left(L_2 i_{2q} + M_m i_{1q} \right); \\ \Delta u_{2q} = R_2 i_{2q} + L_2 i_{2q}^{'} + M_m i_{1q}^{'} + \omega_2 \left(L_2 i_{2d} + M_m i_{1d} \right); \\ \Delta M = J_\Sigma \omega^{'} + p_{\text{п}} M_{\text{c}} - p_{\text{п}}^2 M_m \left(i_{2d} i_{1q} - i_{2q} i_{1d} \right). \end{cases} \tag{4}$$

To continue the calculations, it is also necessary to reduce the absolute values to the equation of the residual function. Thus, the absolute values can be presented by the following equations:

$$V_{u_1} = \frac{1}{2}\left[(\Delta u_{1d})^2 + (\Delta u_{1q})^2\right]; \tag{5}$$

$$V_{u_2} = \frac{1}{2}\left[(\Delta u_{2d})^2 + (\Delta u_{2q})^2\right]; \tag{6}$$

$$V_M = \frac{1}{2}(\Delta M)^2 \cdot \tag{7}$$

According to the gradient descent method for finding the minimum of a function, the system of differential equations for changing parameter estimates is determined by equations:

$$\frac{dR_1}{dt} = -\mu_{R_1}\frac{\partial V_{u_1}}{\partial R_1} = -\mu_{R_1}\left[\Delta u_{1d} i_{1d} + \Delta u_{1q} i_{1q}\right]; \tag{8}$$

$$\frac{dL_1}{dt} = -\mu_{L_1}\frac{\partial V_{u_1}}{\partial L_1} = -\mu_{L_1}\left[\Delta u_{1d} i'_{1d} + \Delta u_{1q} i'_{1q}\right]; \tag{9}$$

$$\frac{dR_2}{dt} = -\mu_{R_2}\frac{\partial V_{u_2}}{\partial R_2} = -\mu_{R_2}\left[\Delta u_{2d} i_{2d} + \Delta u_{2q} i_{2q}\right]; \tag{10}$$

$$\frac{dL_2}{dt} = -\mu_{L_2}\frac{\partial V_{u_2}}{\partial L_2} = -\mu_{L_2}\left[\Delta u_{2d} i'_{2d} + \Delta u_{2q} i'_{2q}\right]; \tag{11}$$

$$\frac{dM_m}{dt} = -\mu_{M_m}\left[\frac{\partial V_{U_1}}{\partial M_m} + \frac{\partial V_{U2}}{\partial M_m} + \lambda\frac{\partial V_M}{\partial M_m}\right]; \tag{12}$$

$$\frac{dJ_\Sigma}{dt} = -\mu_{J_\Sigma}\frac{\partial V_M}{\partial J_\Sigma} = -\mu_{J_\Sigma}\omega'\Delta M\,; \tag{13}$$

$$\frac{dM_c}{dt} = -\mu_M\frac{\partial V_M}{\partial M_c} = -\mu_M p_\Pi \Delta M\,, \tag{14}$$

where

$\mu_{R_1}, \mu_{L_1}, \mu_{R_2}$, μ_{L_2}, μ_{M_m}, μ_{J_Σ}, μ_M are positive coefficients that determine the rate of change in parameter estimates; λ is a weighting factor that determines the relative influence of the residual functions V_{u_1}, V_{u_2}, V_M.

To identify the parameters of the phase and load equivalent circuit, the values of the coefficients μ_{R_1}, μ_{L_1}, μ_{R_2}, μ_{L_2}, μ_{M_m}, μ_{J_Σ}, μ_M are selected according to the nature of the signals $i_{1d}(t)$, $i_{2d}(t)$, $i_{1q}(t)$, $i_{2q}(t)$, $i'_{1d}(t)$, $i'_{2d}(t)$, $i'_{1q}(t)$, $i'_{2q}(t)$, $\omega_1(t)$, $\omega_2(t)$, $\omega(t)$.

Thus, the system of equations (1) is an algorithm of the object of identification, and the system of equations (2)–(7), in combination with Eqs. (8)–(14), is a mathematical model for identifying the parameters of a generalized machine. Figure 2 shows a block diagram of a device for identifying parameters created using the above-mentioned mathematical model.

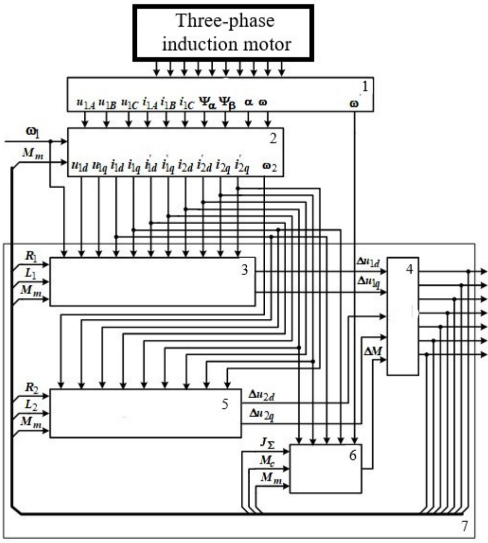

Fig. 2. Block diagram of an asynchronous electric drive with the parameter identification device.

1 – Sensor block. 2 – Coordinate converter.
7 – Parameter identification device, which consists of the following blocks:
3 – Block for calculating the residual stator voltage.
4 – Block of parameter estimates.
5 – Block for calculating the rotor voltage residuals.
6 – Block for calculating the residual torque.

Further, Simulink Simscape Power Systems software (MATLAB tools) is used to confirm that the proposed algorithm is executed correctly and the solution matches the mathematical model with the required degree of accuracy [16].

3.2. Verification of the Mathematical Model

To verify the mathematical model, the AIR80A6U2 motor was chosen as the object of research. The following input data were accepted: voltage $u_{1d}(t)$ =0, and voltage $u_{1q}(t)$ and angular velocity $\omega_1(t)$ changes in accordance with the digital timing diagrams. Figure 3 shows a digital timing diagram, where T1 is a period of a sinusoid (the length of a complete cycle). Function parameters $u_{1q}(t)$ and $\omega_1(t)$ are demonstrated in Table 1. Figure 4 shows the test system for the three-phase induction motor.

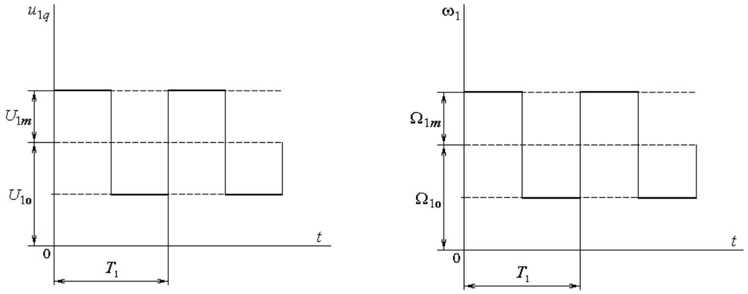

Fig. 3. Digital timing diagrams of functions $u_{1q}(t)$ and $\omega_1(t)$.

Table 1. Function Parameters $u_{1q}(t)$ and $\omega_1(t)$

Parameter name	Function	
	$u_{1q}(t)$	$\omega_1(t)$
Constant component	U_{1o} = 50 V	Ω_{1o} = 300 rad/s
Amplitude of a variable component	U_{1m} = 25 V	Ω_{1m} = 150 rad/s
Frequency of a variable component	f_1= 0.318 Hz	

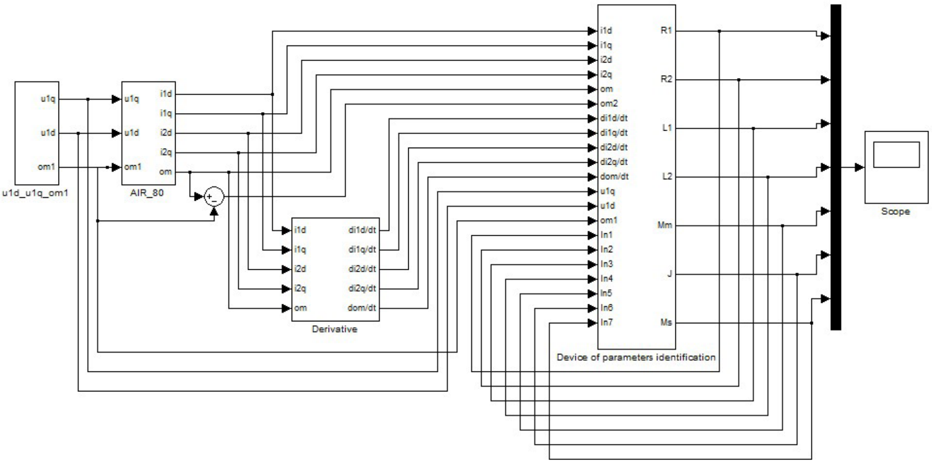

Fig. 4. Test system for the three-phase induction motor.

Thus, to validate the algorithm, deviations of parameters from true values by 50 % and 75 % have been simulated. Relative parameter estimates were introduced to graphically present the results. They are determined by the following equations:

$$R_1^* = \frac{R_1}{R_{1o}}; \quad L_1^* = \frac{L_1}{L_{1o}}; \quad R_2^* = \frac{R_2}{R_{2o}}; \quad L_2^* = \frac{L_2}{L_{2o}}; \quad M_m^* = \frac{M_m}{M_{mo}}; \quad J_\Sigma^* = \frac{J_\Sigma}{J_{\Sigma o}}. \tag{15}$$

In accordance with the Linearization Method proposed in the article "A Novel Method to Monitor and Predict Voltage Collapse: The Critical Transitions Approach", deviations of the parameters from the true values were determined [5].

Graphical presentation of results for deviations by 50 % allows concluding that the relative error is no more than 0.31 % and time of process has a cycle time of 143 seconds. Graphical presentation of results for deviations by 75 % allows concluding that the relative error is no more than 0.23 % and time of process has a cycle time of 209 seconds. In the case of deviation of the parameters from the true values by 50 % and 75 %, all the values are obtained near unity.

Therefore, it can be concluded that the parameters are close to the true values.

Figure 5 shows graphical results for the deviation of parameters from the true values by 75 %. The results of determining the deviations of the parameters from the true values by 50 % and 75 % are presented in Table 2. The initial deviations of the parameter estimates in Fig. 5 are marked with symbol "o". The identification process by time stops when the estimate of all parameters differs from the true values by 0.5 %.

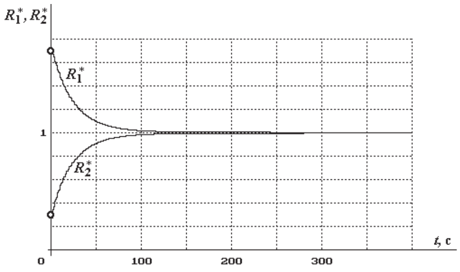

a) stator and rotor winding phase active resistance, Ohm

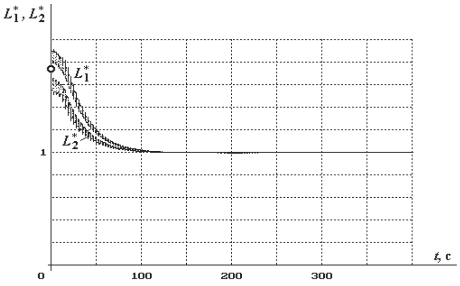

b) stator and rotor winding phase inductance, H

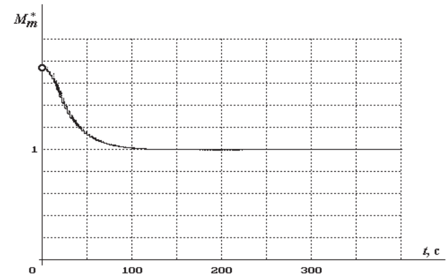

c) mutual inductance between stator and rotor phase winding, H

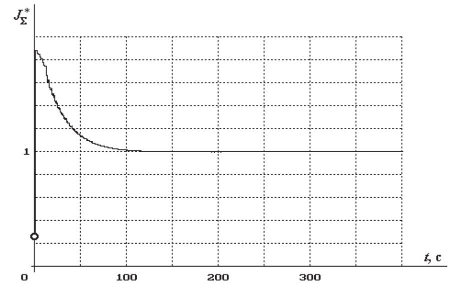

d) moment of inertia of moving parts, kg m^2

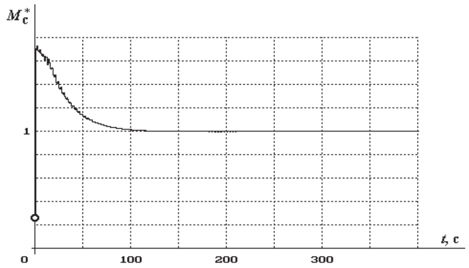

e) static moment of inertia, Nm

Fig. 5. Graphical presentation of results of the deviation of parameters from the true values by 75 %.

Table 2. Results of Computer Simulation of the Identification Process

Parameter name	True parameter values	The result of deviations in the identification of parameters from the true values		Relative error of deviation of parameters from the true values	
		deviation by 50 %	deviation by 75 %	deviation by 50 %	deviation by 75 %
R_1 – Active resistance of the stator winding phase, Ohm	8.9779	9.0035	8.9962	0.28 %	0.20 %
L_1 – Stator winding phase inductance, H	0.5168	0.5156	0.5159	0.22 %	0.16 %
R_2 – Active resistance of the rotor winding phase, Ohm	5.7426	5.7245	5.7291	0.31 %	0.23 %
L_2 – Rotor winding phase inductance, H	0.5194	0.5180	0.5184	0.25 %	0.19 %
M_m – Mutual inductance, H	0.4962	0.4950	0.4953	0.24 %	0.18 %
J_Σ – Moment of inertia of moving parts, kg m^2	0.0250	0.0249	0.0250	0.25 %	0.18 %
M_c – Static moment of inertia, Nm	0.2500	0.2494	0.2495	0.25 %	0.19 %

The analysis of the identification process allows concluding:

- The identification results with the initial deviation from the true values by 75 % show that they are closer to the true values.
- The relative error of the parameters from the true values for deviation by 50 % is higher than for deviation by 75 %.
- The presence of local minima is not established during the verification of the mathematical model.

Verification of the mathematical model allows concluding that the proposed parameter identification method results in the acquisition of theoretically valid results.

3.3. Experimental Testing

The experimental plant is shown in Fig. 7.

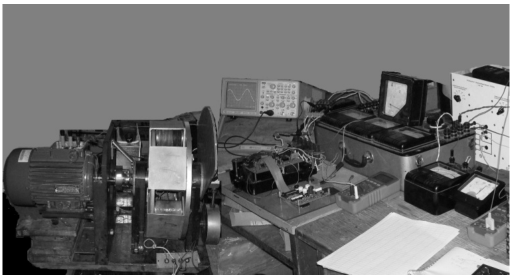

Fig. 7. Experimental plant.

The experimental setup consists of the following:

- AIR80A6U2 three-phase induction motor;
- PS22A73 three-phase frequency inverter (Mitsubishi Electric);
- load device with a torque meter;
- phase voltage and current sensors;
- induction motor with Hall sensors;
- rotation speed sensor;
- analogue-to-digital converter.

The control is carried out using the dsPIC30F3010 microcontroller and the personal computer. Functional diagram of the experimental setup is shown in Fig. 8.

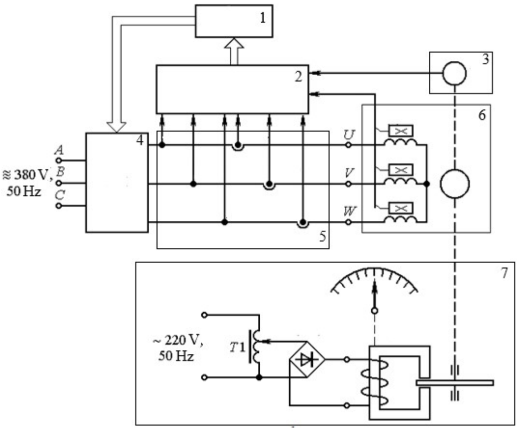

Fig. 8. Functional block diagram of the experimental setup.

1 – Coordinate converter.
2 – Analogue-to-digital converter.
3 – Rotation speed sensor.
4 – Frequency converter.
5 – Phase voltage and current sensors.
6 – Induction motor with Hall sensors.
7 – Load device with a torque meter.

Graphical presentation of results for deviations by 50 % allows concluding that the relative error is no more than 6.71 %, and time of process has a cycle time of 143 (+/- 10 %) seconds.

Graphical presentation of results for deviations by 75 % allows concluding that the relative error is no more than 6.08 %, and time of process has a cycle time of 209 (+/- 10 %) seconds.

Experimental study has time discrepancy with computer simulation less than 10 %.

According to the results of the experimental study, when the parameters deviated from the true values by 50 % and 75 %, a discrepancy from 3.5 % to 6.71 % was found. The results of determining the deviations of the parameters from the true values by 50 % and 75 % are presented in Table 3.

Table 3. Results of Experimental Study of the Identification Process

Parameter name	The result of deviations in the identification of parameters from the true values		Relative error of deviation of parameters from the true values	
	deviation by 50 %	deviation by 75 %	deviation by 50 %	deviation by 75 %
R_1 – Active resistance of the stator winding phase, Ohm	9.2814	9.2930	3.38 %	3.50 %
L_1 – Stator winding phase inductance, H	0.5485	0.5431	6.14 %	5.11 %
R_2 – Active resistance of the rotor winding phase, Ohm	5.9367	5.9430	3.38 %	3.50 %
L_2 – Rotor winding phase inductance, H	0.5540	0.5509	6.65 %	6.08 %
M_m – Mutual inductance, H	0.5295	0.5246	6.71 %	5.74 %
J_Σ – Moment of inertia of moving parts, kg m^2	0.0264	0.0262	5.75 %	4.63 %
M_c – Static moment of inertia, Nm	0.2641	0.2623	5.62 %	4.92 %

3.4. Comparison of the Results and Analysis

Comparing the data given in Table 2 and Table 3, the following results have been obtained:

- The experimental study shows that the relative error of the deviation of the parameters from the true values is 10 times greater than in computer simulation. However, it should be noted that the relative error from the true values is no more than 6.71 %.
- In the computer simulation, the stator winding phase inductance (L_1) has the smallest deviation of the parameters and active resistance of the rotor winding phase (R_2) is the largest for deviation by 50 % and 75 %.
- In the experimental study, the active resistance of the stator and rotor winding phase (R_1 and R_2) have the smallest deviation of parameters for both deviation by 50 % and 75 %. The mutual inductance (M_m) is the highest for deviation by 50 % and rotor winding phase inductance (L_2) for deviation by 75 %.

Table 4 shows the relative error of deviation of parameters from the true values using computer simulation and experimental study.

Table 4. Results of the Identification Process of Relative Error of Deviation of Parameters from True Values

Parameter name	Computer simulation		Experimental study	
	deviation by 50 %	deviation by 75 %	deviation by 50 %	deviation by 75 %
R_1 – Active resistance of the stator winding phase, Ohm	0.28 %	0.20 %	3.38 %	3.50 %
L_1 – Stator winding phase inductance, H	0.22 %	0.16 %	6.14 %	5.11 %
R_2 – Active resistance of the rotor winding phase, Ohm	0.31 %	0.23 %	3.38 %	3.50 %
L_2 – Rotor winding phase inductance, H	0.25 %	0.19 %	6.65 %	6.08 %
M_m – Mutual inductance, H	0.24 %	0.18 %	6.71 %	5.74 %
J_Σ – Moment of inertia of moving parts, kg m^2	0.25 %	0.18 %	5.75 %	4.63 %
M_c – Static moment of inertia, Nm	0.25 %	0.19 %	5.62 %	4.92 %

The comparison allows concluding that the relative errors in the identification of the parameters obtained in the course of the experimental study are higher than the errors obtained in the computer simulation.

The results of the analysis have the following features:

- saturation and steel loss consideration are not taken into account in computer simulations, since an idealized model is used;
- the possibility of using adjustment of the frequency converter is absent in the mathematical model;
- the use of equipment for regulating the frequency converter is not taken into account in the mathematical model.

3. CONCLUSION

Within the framework of the present study, the structure of the algorithm and the mathematical model for evaluating the parameters of the equivalent circuit of an asynchronous electric motor for intelligent monitoring systems have been considered and tested. Gradient descent method and Generalized Theory of Electrical Machines have been used to identify the seven parameters of a three-phase asynchronous motor for intelligent monitoring systems.

Testing allows concluding that the methodology of the algorithm results in the acquisition of theoretically and practically valid results. Taken together, the theoretical and practical studies have shown that the calculated parameters are close to the true values and their cycle time coincides by more than 90 %.

The present study has revealed several opportunities for further research.

First, it is necessary to create an algorithm for identifying squirrel-cage rotor currents to ensure flexibility, stability and reliable operation of a three-phase induction motor.

Secondly, it has also been revealed that mathematical and experimental models for identifying rotor speed parameters without sensors must be created for intelligent monitoring systems.

ACKNOWLEDGEMENTS

The research has been supported by the Ministry of Science and Higher Education of the Russian Federation on fundamental scientific research "Distributed Automated Systems for Monitoring and Diagnosing the Technical Condition of Overhead Power Lines and Substations Based on Technology of Broadband Data Transmission through Power Lines and the Industrial Internet of Things" (theme No. 075-03-2022-151).

REFERENCES

1. Al-Muhaini, M., & Heydt, G.T.A. (2013). Novel Method for Evaluating Future Power Distribution System Reliability. *IEEE Transactions on Power Systems, 28* (3), 3018–3027. doi: 10.1109/TPWRS.2012.2230195.
2. Schuerger, R., Arno, R., & Dowling, N. (2016). Why Existing Utility Metrics Do Not Work for Industrial Reliability Analysis. *IEEE Transactions on Industry Applications*, *52* (4), 2801–2806. doi: 10.1109/TIA.2016.2551696.
3. Kavousi-Fard, A., Niknam, T., Akbari-Zadeh, M., & Dehghan, B. (2014). Stochastic Framework for Reliability Enhancement Using Optimal Feeder Reconfiguration. *Journal of Systems Engineering and Electronics, 25* (5), 901–910. doi: 10.1109/JSEE.2014.00104.
4. Samuelsson, O., Hemmingsson, M., Nielsen, A.H., Pedersen, K.O.H., & Rasmussen, J. (2006). Monitoring of Power System Events at Transmission and Distribution Level. *IEEE Transactions on Power Systems*, *21* (2), 1007–1008. doi: 10.1109/TPWRS.2006.873014.
5. Zheng, L., Hu, W., Min, Y., & Ma, J. (2018). A Novel Method to Monitor and Predict Voltage Collapse: The Critical Transitions Approach. *IEEE Transactions on Power Systems, 33* (2), 1184–1194. doi: 10.1109/TPWRS.2017.2737465.
6. Anagnostou, G., Boem, F., Kuenzel, S., Pal, B.C., & Parisini, T. (2018). Observer-Based Anomaly Detection of Synchronous Generators for Power Systems Monitoring. *IEEE Transactions on Power Systems, 33* (4), 4228–4237. doi: 10.1109/TPWRS.2017.2771278.
7. Ye, H., Song, W., Ruan, Z., & Yan, Y. (2019). Current control methods for dual three-phase permanent magnet synchronous motors considering machine parameter asymmetry. In: *22nd International Conference on Electrical Machines and Systems (ICEMS),* (pp. 1–6), 11–14 August 2019, Harbin, China. doi: 10.1109/ICEMS.2019.8921516.
8. *Press, W. H., Teukolsky, S. A., Vetterling, W. T., & Flannery, B. P. (1992). Numerical Recipes in C: The Art of Scientific Computing (2nd ed.). New York: Cambridge University Press.*
9. *Barzilai, J., & Borwein, J.M. (1988). Two-Point Step Size Gradient Methods. IMA Journal of Numerical Analysis, 8 (1), 141–148. doi:10.1093/imanum/8.1.141.*
10. Salimin, R. H., Binti Abd Kadir, S.H., Mohd, S.R., Baki, S., & Ismail, F. Parameter identification of three-phase induction motor using MATLAB-simulink. In: IEEE 7th International Power Engineering and Optimization Conference (PEOCO), (pp. 647– 651), 3–4 June 2013, Langkawi. doi: 10.1109/PEOCO.2013.6564627.
11. Parsley, G.M.J., Meyer, A.S., & Landy, C.F. (1993). The prediction of the commutation performance of direct current machines using a combination of magnetic finite element analysis and the principles of generalised machine theory. In: *1993 Sixth International Conference on Electrical Machines and Drives* (Conf. Publ. No. 376), (pp. 38–43), Oxford, UK.

12. Ivanov-Smolensky, A. V. (1980). *Electrical Machines*. Moscow: Energy.
13. Kopylov, I.P. (2001). *Mathematical Modeling of Electrical Machines*. Moscow: Higher school.
14. Morgan, A.T. (1979). *General Theory of Electrical Machines*. Bristol: Heyden.
15. Adkins, B., & Harley, R.G. (1979). *The General Theory of Alternating Current Machines*. London: Chapman and Hall.
16. MathWorks. (n.d.) *Simulink SimPowerSystems.* Available at https://uk.mathworks.com/products/simpower.html

LATVIAN JOURNAL OF PHYSICS
AND TECHNICAL SCIENCES
2022, N 2

DOI: 10.2478/lpts-2022-0010

STUDY ON POTENTIAL ROLE AND BENEFITS OF LIQUIFIED NATURAL GAS IMPORT TERMINAL IN LATVIA

A. Ansone*, L. Jansons, I. Bode, E. Dzelzitis, L. Zemite, A. Broks

Riga Technical University,
Faculty of Civil Engineering, Institute of Heat,
Gas and Water Technology,
6B/6A Kipsalas Str., Riga, LV-1048, LATVIA
*e-mail: ansoneance@gmail.com

Natural gas is relatively clean energy source, which emits less greenhouse gases (hereinafter – GHG), compared to other fossil fuels, such as hard and brown coal, and therefore it may be the most feasible resource to ensure smooth energy transition towards Europe's climate neutrality by 2050. Traditional natural gas can be easily transported and used in liquefied (hereinafter – LNG) or compressed form. As for biomethane, in future it also can be used in liquefied (hereinafter – bioLNG) and compressed form, as well as transported by means of the current natural gas infrastructure. It can also significantly enhance regional and national energy security and independence, which has been challenging for the European Union (hereinafter – EU) over at least several decades.

Issue on energy independence, security of supply, alternative natural gas sources has been in a hotspot of the Baltic energy policy makers as well. Now, considering Russia's invasion in Ukraine, since late February 2022, a problem of the EU natural gas dependency on the Russian Federation has escalated again and with force never before experienced. The European natural gas prices also hit records, as the natural gas prices in the Netherlands Title Transfer Facility reached 345 euros per megawatt-hour (hereinafter – EUR/MWh) in March 2022.

Therefore, LNG import terminal is the only viable option to reduce national dependency of the so-called pipe gas which in some cases, due to the insufficient interconnections, may be delivered from very limited number of sources. The European policy makers and relevant institutions are currently working towards radical EU natural gas supply diversification, where LNG deliveries coming from outside of Russia will certainly take a central stage.

In case of Latvia, the potential benefits of the LNG terminal development in Skulte were evaluated in order to reduce energy independence of the Russian natural gas deliveries in the Baltic region and to introduce new ways and sources of the natural gas flows to the Baltics. LNG terminal in Skulte could ensure significant capital investment cost reduction comparing to other projects proposed for Latvia in different periods, due to already existing natural gas transmission infrastructure and the relative closeness to the Incukalns underground gas storage (hereinafter – UGS). Various aspects, such as technical, political and economic ones, were analysed to assure that Skulte LNG terminal would be a real asset not only to customers of Latvia, but also to those of the whole Baltic region, where in future it would be possible to use biomethane for efficient utilisation of existing and developing natural gas infrastructure.

Keywords: *Biomethane, energy independence, energy policy, energy security, gas storage, gas transmission, LNG, security of supply, SoS.*

1. INTRODUCTION

The European Green Deal is a set of the EU policy initiatives, which was approved in 2020, with the main goal to reach Europe's carbon-neutrality by 2050. This requires major changes in energy sector as well, especially considering *Fir-for-55* legislation package, which was published in July 2021, setting policy measures to reduce EU's GHG emissions by 55 % comparing to year 1990 [1].

Natural gas is also considered to be sustainable under the EU's Taxonomy Regulation delegated act, published in February 2022, which classifies economic activities that are sustainable, to help investors and any other party better shift investments towards sustainable development. According to the European Commission (hereinafter – EC), the natural gas facilities have to comply with strict rules and, in case of fossil gas related activities, should switch to renewable gases (hereinafter – RG) by the end of 2035 [2]. In the future, where fossil natural gas might be fully substituted by the RG biomethane, potential biomethane supply could be arranged not only by using current natural gas transmission and distribution systems, but also by sea in a form of bioLNG [3].

Any LNG can be used in several crucial sectors of the national economy in order to provide reliable and clean energy: for example, it can help imeet energy needs of freight and maritime transport sectors and provide environmentally sound and affordable fuel for electric energy and heat generation [4]. Especially, in regions where renewable energy sources are less available or cannot meet high energy demand in winter season [5]–[7].

2. THE NATURAL GAS SUPPLY RISKS IN THE BALTIC REGION

2.1. Import and Supply Sources

More than a decade ago, the Baltic States asked the EC to help find compromise on LNG terminal construction location in the Baltic region, but the initiative failed to find a common ground on development and cost sharing [8]. The only one of the Baltic States, which actually developed its own national LNG import terminal project, was Lithuania, and the Klaipeda LNG terminal was commissioned in 2014. Its import capacity reaches 3.75 billion cubic meters (hereinafter – BCM; around 36.64 terawatt-hours (hereinafter –TWh)) per year. Unfortunately, 90 % of the Europe's natural gas is imported [9]. Share of each exporting country in the EU's natural gas import is shown in Fig. 1.

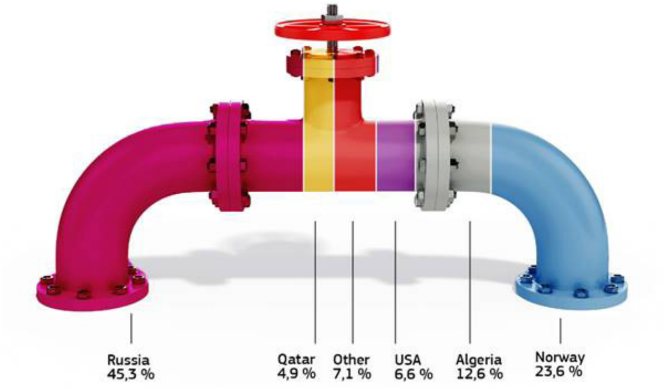

Fig. 1. The EU natural gas imports [10].

In 2021, around 140 BCM (around 1367.72 TWh*) of natural gas were imported to the EU by pipelines, while 15 BCM (146.54 TWh*) were delivered as LNG [11]. The Baltic States and Finland still relied mostly on the natural gas supplies from Russia, while Lithuanian natural gas supplies were more diverse due to the ever-growing natural gas imports though Klaipeda LNG terminal [12].

Once again, a question on the natural gas supply and Europe's dependency on Russian gas has escalated, considering Russia's invasion in Ukraine, which started in February 2022. The European natural gas prices also hit records, as the natural gas prices in the Netherlands Title Transfer Facility reached 345 EUR/MWh in March 2022 [13].

In a short-term period, the EC plans to minimise Russian natural gas dependency by means of increasing the share of the LNG import from the USA and Qatar, while in a longer run, it is working towards additional alternatives, including locally produced RGs, such as biomethane or hydrogen. In March 2022, the International Energy Agency also revealed a plan to reduce the EU's dependency on the Russian natural gas supplies, where one of the key suggestions was to replace Russian pipeline natural gas supplies with non-Russian LNG ones. In comparison to 2021, it would be possible to increase LNG import to the EU by 50–60 BCM per year, but since suppliers were more or less the same, it might result in higher LNG prices worldwide [11]. On 8 March 2022, the EC introduced communication on a new plan "REPowerEU: Joint European Action for more affordable, secure and sustainable energy" to become independent of Russia's fossil fuel, which includes LNG import diversification, using a wider range of potential suppliers, including but not limited to Qatar, the USA, Egypt and West Africa [10].

While diversifying the EU's natural gas supplies in a form of LNG, the role of UGSs is tend to grow in foreseeable future. The Baltic region has only one such a storage – Incukalns UGS located in Latvia, which is also one of the most modern UGS facilities of its type in Europe with a capacity of 2.3 BCM. It can ensure safe storage of the large amounts of natural gas that has been imported to Latvia and the whole Baltic region. Therefore, LNG terminal in Latvia could not only increase security of supply in our country, but also in the remaining Baltic countries and Finland.

2.2. Main Aspects of Analysis of the Baltic Natural Gas Supply Risks

At the end of 2021 and beginning of 2022, the EU natural gas market was under tension, where atypically high natural gas demand was observed. However, at that time it was translated as global economic recovery from the pandemic. While Russia's war against Ukraine escalated, in March 2022 the natural gas flows from Russia via Yamal pipeline (via Belarus and Poland) to Germany declined sharply. Possible reason is that keeping Russia's supplies low would highlight a need for additional routes, such as commissioning of currently banned the Nord Stream 2 pipeline project [14]–[16].

There was a hope that the natural gas supply risk plans that were developed under Regulation (EU) 2017/1938 of the European Parliament and of the Council of 25 October 2017 concerning measures to safeguard the security of gas supply and repealing Regulation (EU) No. 994/2010 (hereinafter – Regulation 2017/1938) would not be used in real life, while ongoing war in Ukraine and the EU sanctions proved that scenarios from the preventive action plan and emergency plan could actually came true in foreseeable future [17].

In a preventive action plan, one of the scenarios simulates a situation where, due to the geopolitical crisis, the flow of natural gas from Russia stops completely within two weeks of peak demand and eight average winter weeks. The most significant risks identified in the preventive action plan are related to the natural gas supply disruptions from Russia in March coupled with insufficient natural gas reserve in Incukalns UGS. Among others, it was concluded on the national level that the limiting factor of the natural gas transmission system is the cross-border interconnection capacity. The amount of active gas stored at the Incukalns UGS is the most important factor in guaranteeing both the Latvian and regional security of the natural gas supply. Lithuania's support to Latvia in some crisis scenarios is limited by the potential volatility of the LNG cargos due to LNG logistics [18].

An important role in the Baltic natural gas supply is dedicated to the Polish–Lithuanian natural gas interconnector (hereinafter – GIPL), which will be commissioned in mid-2022, ending isolation of the Baltic States from central European natural gas transmission systems, but unfortunately no plan predicted limited natural gas supplies from Russia to the whole Europe at the same time, as it is happening now. With high geopolitical tensions in relations with Russia for at least midterm perspective, the only viable option for the natural gas supplies to the Baltic States and Finland is Klaipeda LNG terminal and GIPL. In accordance with early warning in the natural gas supply sector of Latvia that was announced on 9 March 2022, the natural gas deliveries from Klaipeda LNG and via GIPL are regarded as prioritising gas flows by the Latvian natural gas transmission system operator (hereinafter – TSO) Conexus

Baltic Grid [19]. However, before finishing enhancement of the Latvia–Lithuania interconnection (ELLI project) in 2024, current interconnection capacities and operating pressures are limited between Lithuania and Latvia (known as the bottleneck effect), therefore making it challenging to provide absolutely sufficient natural gas supplies to Latvia, Estonia and Finland from the Lithuanian and Polish side [20], [21].

The necessary natural gas reserve of capacity in the region is provided by Incukalns UGS, which allows fully compensating for seasonal fluctuations (except for Finland, which has to adjust the demand for maximum hours to the capacity of *Balticconnector*). Nevertheless, the total amount of available capacity at the Klaipeda LNG and GIPL entry points per year may be lower than demand, depending on climate conditions and industrial demand. It addresses an important question of necessity to create at least one more LNG import terminal in the Baltic region in the shortest possible terms.

A number of traders may seek to diversify supply risks in the market as well. However, there is a significant market power, currently on the part of supplies from Russia, as well as on the part of the Baltic region industrial energy companies, which maintain a high level of concentration. Market power discourages investments by private investors, relying solely on expected demand for the natural gas import capacity. Also, high volatility of the energy prices with construction and development time delays discourages private investors. Markets with high levels of concentration and/or with signs of market power, show a significant increase in risk, which discourages private capital from making significant investments [22]. Therefore, the Baltics States and Finland, since having high market power from Russia's gas, have low chances of fully-private investment in the natural gas supply diversification projects.

3. TECHNICAL ASPECTS OF LNG TERMINAL BUILDING PROJECT IN LATVIA

3.1. Site Selection Evaluation for Potential LNG Terminal in Latvia

Latvia, as all the Baltic countries and Finland, is located on the shores of the Baltic Sea, with the coast line more than 450 kilometres long. When planning LNG terminal construction, various aspect should be considered, such as closeness of the port cities, accessibility of the infrastructure (transmission pipelines) and distance to Incukalns UGS. Therefore, originally three potential locations of the LNG import terminal were reviewed in Latvia: Ventspils (with existing oil pipelines and port), Riga (port) and Skulte (port). The comparison of the three chosen locations is shown in Table 1.

In general, it is believed that Skulte is the best of the three possible locations with several significant benefits:

- geographical closeness to Incukalns UGS;
- easy access and safe maneuvering of the LNG vessels;
- adequate terminal and pipeline routing separation from the residential areas;
- lacking interference with the existing ship traffic;
- ice-free port for most of the year;
- no urgent need for LNG storage tanks (with regard to closeness of Incukalns UGS) [23].

Table 1. Comparison of Potential Locations of LNG Import Terminal in Latvia

Location	**Ventspils**	**Riga**	**Skulte**
Solution/costs	Port infrastructure is suitable only for onshore solution that has high CapEx	Port infrastructure is suitable only for onshore solution, which has high CapEx	Port location is suitable for FSU, which is the most effective cost solution
Consumption	Potential new consumption by port companies and city	Location close to the biggest end consumers in the country	Close location to Incukalns UGS that is the key infrastructure element in the region
Ice conditions	Ice free port	Port has the biggest ice coverage in Latvia	Port has average ice coverage in winter months
Grid connection	Investments are required to upgrade existing oil transportation pipeline (200 km) and connection to the grid	Residential area around the port makes the pipeline routing to grid (16 km) difficult. Distance to Incukalns UGS is 50km	Pipeline distance to Incukalns UGS is 30– 35 km. The route is crossing rural areas
Vessel traffic	Terminal location is in the navigable area of the port that makes interference with the main traffic	Terminal location is in the navigable area of the port that makes interference with the main traffic	Terminal is located outside navigable area
Flexibility	Long distance to the Incukalns UGS makes the low flexibility in supplies	Absence of direct connection to UGS lowers flexibility of supplies. In winter period, it is possible to absorb the regasified gas in the natural gas distribution system	Very high flexibility because of direct connection to Incukalns UGS
Other		Process of land rent agreement allocation lacks transparency	Substantial support from port authorities

3.2. Evaluation of Potential LNG Terminal Concepts

Various LNG terminal types were compared in order to find the most suitable LNG import terminal solution that could ensure both security of the natural gas supply for Latvia and the Baltic region, and provide relatively low operational costs of the terminal. The general estimate is shown in Table 2.

Table 2. Comparison of Potential LNG Import Terminal Concepts

Criterion	**Onshore terminal**	**Floating Storage Regasification Unit (FRSU)**	**Floating Regasification Unit (FRU)**
Costs	Highest CapEx because of extensive ground building (infrastructure and storage tanks)	Relatively high CapEx because of vessel use and storage tank placement on the vessel	Low CapEx because of simple technical solution – floating platform with regasification equipment
Operational costs	High operational costs because of extensive onshore storage and infrastructure maintenance	Relatively high operational costs because of storage tank and vessel maintenance	Low operational costs because of simple technical solution. No costs on standby mode
Flexibility	Low flexibility because of limited storage capacity	Low flexibility because of limited storage capacity	High flexibility because of direct connection to Incukalns UGS
Freight speed	It takes 2–3 days to unload the LNG vessel	It takes 2–3 days to unload LNG vessel	It takes about 6–8 days to unload LNG at planned capacity (can be increased)
Timing	The building of such a terminal takes 6 or more years	The building of such a terminal takes 4 or more years	The project execution time is estimated to be less than 2 years after final investment decision

Floating regasification unit (hereinafter – FRU) could ensure the lowest costs to the energy consumers, due to the low operational costs, relatively simple technology and no need to store the natural gas on site. FRU consists of a tubular structure where the columns contribute most to the buoyancy required. Due to the small and distributed water plane area the floater will have very stable sea keeping characteristics. Due to the tubular structure the displacement of the floater is low compared to the conventional ship shaped or barge solution and thus low steel weight; this has a direct positive impact on the construction and maintenance cost of the floater. Mooring of the floater at site could be conventional spread mooring. The visiting LNG carriers could be moored to the floater with conventional ship-to-ship mooring methods. These methods are in accordance with the tried and tested industry practices.

3.3. Technical Aspects of Potential LNG Terminal in Latvia

For the Skulte LNG import terminal, natural gas storage is considered to be at the Incukalns UGS. This, in principle, makes the requirement for on-site LNG storage redundant and thus brings down the project capital expenditures (hereinafter – CapEx) to as low as 1/3 to 1/4 of the other projects proposed in the Baltic Sea region.

Implementation of Skulte LNG import terminal, using FRU solution, will mean that LNG shall be pressurized, vaporized and sent-out to a medium pressure subsea gas pipeline and onshore gas pipeline to Incukalns UGS. The project also would include the subsea pipeline and the onshore pipeline carrying natural gas from the terminal to either existing gas transmission system or the UGS facility. The general technical information of Skulte LNG terminal is summarised in Table 3.

Table 3. General Technical Information of Skulte LNG Terminal [23]

Terminal capacity	Up to 3 million tonnes/year
Regasification capacity	600 million standard cubic feet of gas per day
Storage	Existing UGS at Incukalns Latvia with capacity of 2.3. BCM
Supply LNG carrier size	40 000 m^3 to 170 000 m^3
Carried offload time	4 to 8 days at full capacity

The key element of the Skulte LNG import terminal concept is direct pipeline to Incukalns UGS, whose technical parameters must be in line with terminal regasification capacity and gas transportation pressure in the grid. The preliminary technical parameters for pipeline are provided in Table 4.

Table 4. Preliminary Technical Parameters for Pipeline Connecting Skulte LNG and Incukalns UGS

Transmission capacity	15–20 million m^3/ day
Pressure	55 bar
Diameter	0.7 m

4. SITUATION EVALUATION IN THE BALTIC REGION

4.1. The Overview of Natural Gas Market

In the Baltic region, the natural gas demand is historically dominated by power and heat generation and industrial consumption, thus creating sensitivity to price fluctuations. The natural gas consumption in the Baltics between 2015 and 2020 is shown in Fig. 2.

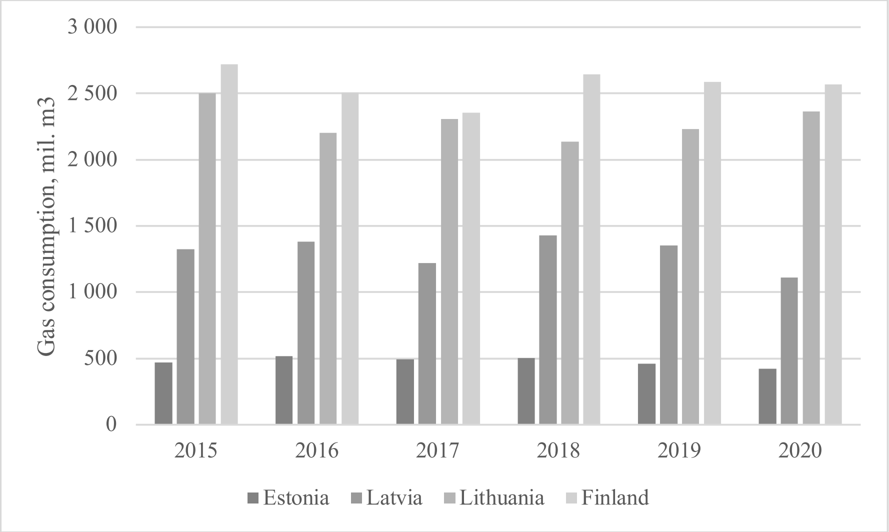

Fig. 2. The natural gas consumption in the Baltic States (2015–2020) [24].

Source: *Eurostat*

The largest natural gas consumers in the Baltic States are AB Achema (latgest fertilizer producer in Baltic States, located in Lithuania), JSC Latvenergo (state-owned energy company that generates about 70 % of the electric energy in Latvia), AB Lietuvos Elektrinės (the owner of the Elektrėnai Power Plant in Lithuania), JSC Nitrofert (the only fertilizer producer in Estonia), JSC Rigas Siltums (the district heating company of Riga, Latvia), and other district heating companies. However, future trends of the natural gas consumption in the Baltics could be affected by increased LNG use. Namely, the usage of natural gas could increase and penetrate brand new sectors of the national economies. There is a large potential for LNG to be used as truck fuel – a cleaner alternative comparing to diesel [4].

It is not easy to assess the future position that natural gas will play in the energy mix of the Baltic States. The trends of natural gas consumption are influenced by the overall development of the national economy, building energy efficiency development, the use of modern and economical gas burning equipment and gradual replacement of the natural gas with RGs [25].

4.2. Evaluation of LNG Projects in the Baltic Region

According to various sources, at least ten potential LNG import terminal locations were considered throughout the Baltic region: Liepaja, Ventspils, Riga, Skulte/Lilaste (all in Latvia), Paldiski, Muuga, Sillamae (all in Estonia), Inkoo and Turku (both in Finland). Five projects (Skulte, Paldiski, Talinn, Muuga and Inkoo) have reached a certain development maturity stage to foresee a possibility to be actually implemented [26].

Some projects are dependent on the EU funding, therefore, need to meet Projects of Common Interest criteria. From these potential projects, only Skulte LNG terminal has an immediate effect on the natural gas supply portfolio of the Baltic region, both in terms of security of supply and supply diversification. It is located in the middle of the Baltic region, and it can supply natural gas to its neighbouring countries immediately after its commissioning without major investments in the additional natural gas pipeline infrastructure.

In order to outline competitiveness of Skulte LNG terminal project, four existing and planned LNG terminal projects were compared in accordance with several criteria, summarised in Table 5. These terminals are: floating storage and regasification terminal in Klaipeda, onshore terminal with lowered storage capacity in Riga, floating regasification terminal in Skulte and onshore terminal with full storage capacity in Paldiski/Inkoo.

Since three different technologies are involved, for clarity purposes the following assumptions are made:

- an onshore storage tank costs are 1 million EUR per 1000 m^3 of storage capacity;
- regasification unit costs are 50 million EUR;
- mooring costs are 10 million EUR regardless of type of technology used;
- transmission network upgrades and connection to UGS are covered by system charges and EU financial instruments (with 50 % gap) and not by LNG terminal operator;
- unloading freight time is included in case of floating regasification unit technology;
- 20-year period is used for financial calculation, except for Klaipeda (10-year lease);
- 8 % annual return rate for investments is used for all terminals;
- 10-ship scenario is used as a base scenario for regasification cost comparison and 20–5 ship scenario is used to demonstrate flexibility cost of the terminal (penalty for low utilisation compared to high utilisation);
- Freight cost is assumed to be 60 000 EUR per day.

Based on assumptions explained before, Table 1 indicates that since Skulte LNG terminal would not need storage tank (since it is possible to efficiently use Incukalns UGS, if transmission interconnection is built), it would reach total costs of about EUR 60 million, while other projects would cost from EUR 260 to 430 million, making Skulte LNG significantly cheaper and more cost-effective than other LNG terminal projects under review in the Baltic region.

Table 5. Evaluation of LNG Projects in the Baltic Region

Location, Annual regasification capacity (50 % utilisation rate)	**Technology**	**Storage tank**	**Unload costs**	**Supply agreements**	**Financial structure**	**Total gap**	**Total cost at 1 BCM scenario**
Klaipeda, 2 BCM	FSRU	170 000	Indirect – shutdown of other terminals in the port	ToP agreements are crucial – no flexibility available for the terminal (additional storage capacities of flexible consumption)	10-year financial lease with a mandatory market share	NA	Total cost: EUR 430 million; regasification cost: 46 EUR/1000m^3
Riga, 2 BCM	Onshore	200000	No costs associated	To achieve reasonable capacities ToP agreements are needed for operation but partly it could be operated on the opportunistic basis	Not defined but considerable gap (75 %) of financial resources should be covered by public funding	195 million EUR	Total cost: EUR 260 million; regasification cost: 26.4 EUR/1000m^3 Regasification cost with covered gap: EUR 11.85/1000m^3
Skulte, 2 BCM	FRU	N/A	Unloading freight costs	Opportunistic trade mainly, due to low cost of flexibility and ability to operate with irregular shipment schedule	Commercial offtake coverage with limited (33 %) or favourably no market gap for optimal level of utilisation	20 million EUR	Total cost: EUR 60 million; regasification cost: EUR 12.4/1000m^3 Regasification cost with covered gap: EUR 10.6/1000m^3
Inkoo, 2 BCM	Onshore	300000	No costs associated	ToP agreements mainly and limited amount of opportunistic trading	Not defined, but existing available market for power generation, industrial and transport sector; nevertheless, gap (33 %) of financial resources should be covered by public funding	120 million EUR	Total cost: EUR 360 million, regasification cost: EUR 35.4/1000m^3 Regasification cost with covered gap: EUR 24.6/1000m^3

5. POLITICAL AND REGULATORY PERSPECTIVES OF LNG DEVELOPMENT IN LATVIA

5.1. Energy Market Regulation

Most of energy market activities are regulated businesses in Latvia. Market operators in power, natural gas and district heating industries shall obtain license from the Public Utilities Commission. LNG terminal operation, the natural gas transmission and the natural gas trade are among licensed activities. Currently there are 28 natural gas traders in the Latvian natural gas market [27]. Framework of the natural gas market in Latvia is shown in Fig. 3.

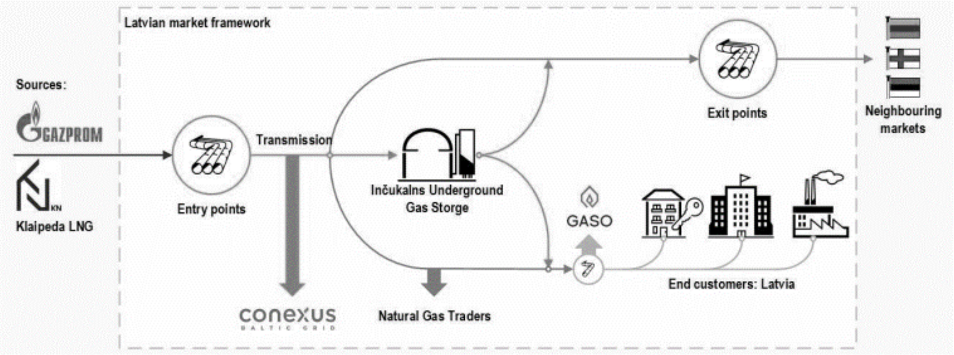

Fig. 3. Framework of the natural gas market in Latvia [28].

Source: *JSC Conexus Baltic Grid*

If developed, Skulte LNG terminal will need to acquire LNG operation license and the natural gas transmission license to operate FRU and connector pipeline to Incukalns UGS. Since 2020, when the single natural gas market in the Baltics has been launched, it unites the natural gas TSOs of Finland, Latvia, and Estonia – Gasgrid Finland, Elering, and Conexus, confirming the cooperation capability of several neighbouring countries. The common natural gas market is characterised by unified entry-exit tariff area, and single Estonian–Latvian balancing zone, while continuously cooperating would ensure deeper integration with prospects of Lithuania joining the market as well [29].

5.2. Access to the Infrastructure

The Energy Law (hereinafter – EL) provides non-discriminatory, tariff-based third-party access to the natural gas infrastructure [30]. Capacity allocations, congestion management and different capacity reservation products are provided by the national transmission and storage network code. Selling capacity reservation products in secondary market is allowed. For the time being short-term capacity reservation products (up to one year) are the most popular in the market. However, long-term capacity reservation products can be designed by the TSO should there be interest from market participants.

Due to a high level of infrastructure integrity and importance of security of the natural gas supplies for the national economy, prices for the natural gas infrastructure services are regulated by tariffs in accordance with the Law On Public Utilities Regulators [31]. Tariff structures are changing from cost plus to revenue cap patterns with numerous variations.

The EL also provides an exemption from general third-party access regime for new infrastructure projects. Conditions for such an exemption are as follows:

- the investment must enhance competition in the natural gas supply and enhance security of supply;

- the level of risk attached to the investment must be such that the investment will not take place unless an exemption is granted;
- the infrastructure must be owned by a natural or legal entity that is separate at least in terms of its legal form from the system operators, in whose systems that infrastructure will be built;
- charges must be levied on users of that infrastructure;
- the exemption must not be detrimental to competition or the effective functioning of the internal market in natural gas, or the efficient functioning of the regulated system, to which the infrastructure is connected.

The national regulatory authority grants the exemption, if *ex ante* verification from the EC is received. Detailed procedure and evaluation criteria for the exemption are stipulated in Directive 2009/73/EC of the European Parliament and of the Council of 13 July 2009 concerning common rules for the internal market in natural gas and repealing Directive 2003/55/EC [32].

Skulte LNG Terminal operator may need to secure third-party access to the terminal and the natural gas transmission via a connector pipeline. Therefore, it is to be decided whether Skulte LNG terminal project operator will apply for derogation from third-party access or not.

5.3. LNG Project Characteristics and Risks

LNG projects possess characteristics and risks that tend to amplify the potential for high value disputes. Such projects are highly technically challenging (including floating LNG technology) and require a myriad of sub-contractors, often based across multiple jurisdictions. They are environmentally sensitive and subject to stringent regulatory requirements. LNG projects are often politically sensitive and subject to significant public scrutiny. LNG projects involve very significant upfront capital expenditure, with essentially no income generation prior to project commissioning [33]. Moreover, the overall viability of an LNG project, which may have an expected lifetime exceeding 30 years, will often depend upon the long-term stability and predictability of regulatory, political and economic environments [33], [34].

For liquefaction and regasification projects in particular, the risks associated with them include: project economics, environmental approvals and regulation, political risks, joint venture risks, technical engineering, procurement and construction challenges, feedstock challenges and end product marketing and contracting. All of the above risks can affect heavily an LNG project and lead to disputes. Successfully addressing project implementation challenges on all levels can be critical to prospects of every LNG import project [35].

5.4. Construction of the Infrastructure Objects

There are a number of stages (phases) to any LNG terminal project, which commonly include, but are not limited to:

- planning and regulatory approvals;
- front end engineering and design (FEED);
- construction;
- construction of related infrastructure (connecting pipelines);
- commissioning and handover;
- post-commissioning operations [35].

However, in many cases, they can be reduced to only two general phases – the exploration / engineering and construction phase (also associated with pre-final investment decision (FID) and post-FID phases [36]). Execution of both phases is regulated by specific laws, and Skulte LNG terminal project implementation shall include both phases.

Exploration phase for the LNG terminal and underwater floating regasification unit connection to pipeline begins with the acquisition of seabed exploration permit. The National Sea Environment Protection and Management Law [37] provides that right to exploit and, consequently, to explore seabed that shall be tendered. However, according to Ports Law [38] no tendering is applicable if seabed exploitation is planned within sea territory allocated as territory of the port. Location of Skulte LNG terminal is planned within territory of Skulte Port subject to an agreement with the port authorities. It is expected that no tendering procedures will be necessary to gather seabed exploration permit and further exploitation of a respective area.

Construction and operation of the LNG terminal may have a direct and material impact on the environment. Environmental Impact Assessment Law (hereinafter – EIA), provides two types of environmental impact assessment, initial assessment and full assessment [39]. The EIA provides a list of activities that are subject to a particular type of assessment. However, further full assessment of a potential activity may be required if results of initial assessment reveal the need for that. Initial assessment is executed by the state institution, Regional Environmental Administration, within 20 days from the receipt of all documents from activity promoters. Full assessment shall be executed by a licensed assessor. Usually, it takes about 8–12 months to complete. Operation of LNG terminal is an activity with advanced safety requirements; therefore, it is expected that it will be subjected to, at least, an initial assessment of environmental risks. Positive conclusion of initial or full environmental assessment is a prerequisite for further project implementation.

Building of the natural gas transmission pipeline is an activity with a material environmental impact according to the EIA.

At the same time, the EL confers to energy infrastructure operators a right to use third-party land to set up an infrastructure object. It prescribes two options on the acquisition of such a right. The first option is to contract with landowners on the right to use their land. The second option is the acquisition of the right to use the land irrespective of landowners' consent, if one of following requirements is met:

- building of an infrastructure object is provided in a zoning plan of a respective municipality;
- municipality has confirmed that an infrastructure object is of public interest and particular land plots are necessary to build it;
- an infrastructure object has status of an object of the national interest. The EL provides that in all above cases landowners shall get compensation from infrastructure developers for use of their property [30]. Amount of remuneration is calculated according to regulations of the Cabinet of Ministers.

Possible routes of Skulte LNG connector pipeline are planned mainly through agricultural land plots. Major part of private land plots to be crossed by the pipeline is used for farming purposes and most of them shall remain as agricultural land after pipeline is built. Landowners therefore shall not suffer material damages and legal restrictions to use their property.

Design and construction of underwater

floating regasification unit connection and connector pipeline is subject to the Construction Law [40] and regulations, which specify that building permits shall be issued by relevant municipalities. However, a single building permit shall be issued by the State Construction Control Bureau of Latvia for objects of the national interest with no right for municipalities to object.

5.5. Object of the National Interest

According to the Spatial Development Planning Law of Latvia (hereinafter – SDPL), objects of national interest are objects securing material public interests, protection and sustainable use of the natural resources. Skulte LNG terminal and transmission pipeline might qualify for the status [41]. Currently major part of natural gas for the Baltic countries is sourced in Russia; thus, recent geopolitical developments in Russia and Ukraine have exposed vulnerability and volatility of this source.

Skulte LNG terminal project would allow sourcing LNG from various suppliers worldwide, such as Norway, the USA, Qatar, Algeria, Nigeria, Trinidad and others. Two of the most likely routes could be from the USA or Norway, as shown in Fig. 4.

Fig. 4. Potential import routes from North America and Hammerfest, Norway.

Source: *JSC Skulte LNG Terminal*

The SDPL provides that the Cabinet of Ministers may confer status of an object of the national interest upon proposal of a competent ministry [41]. For Skulte LNG project, it is the Ministry of Economics. The main advantages of having this status are as follows: challenging building permits for such an object does not stop the building process, energy supply companies acquire statutory right to use third-party land for building of an object of national interest. Such a status would ensure faster and smoother project development, which would be valuable in circumstances, when all the Russian gas import must be reduced to the bare minimum or even completely ceased. In this case, LNG import terminal development in Skulte would ensure fast and efficient natural gas supply routes and source diversification for Latvia [42].

6. CONCLUSIONS

LNG import terminal would help reduce dependency on the pipeline natural gas supplies which, in some cases, due to the insufficient interconnections, may be delivered only from one or limited number of sources. In the context of Latvia, it was evaluated that there was a potentially beneficial role of the LNG terminal development in Skulte, which would help strengthen energy independence of the whole Baltic region as well as introduce new natural gas delivery sources in a cost-efficient way.

LNG terminal in Skulte could also ensure significant capital investment cost reduction compared to other LNG projects in the region, due to already existing infrastructure and the relative closeness of Incukalns UGS. It can also be characterised by easy access and safe manoeuvring of the LNG vessels, adequate terminal and pipeline routing division from the residential areas.

The main benefits of Skulte LNG project are low CapEx compared to other projects proposed in the neighbouring counties. Low cost will be benefitting costumers, while price effect will ensure flexibility of supply provided by terminal direct connection to Incukalns UGS that will ensure direct impact on the price. In addition, it will provide possibility for potential traders to buy LNG in spot market in the favourable time periods.

FRU is the most suitable terminal solution for Latvia because of low CapEx, high flexibility and fast project execution time. Direct pipeline connection to Incukalns UGS can provide possibility to avoid building LNG storage tanks onshore that is often the major part of import terminal costs.

To sum up, there is a need for additional natural gas delivery sources, and LNG terminal in Latvia would help the Baltic region with it. If the natural gas security of supply is a national priority, there is a need for public investment in LNG import projects, which can be implemented in the shortest possible terms, with ability to guarantee stable, secure and diversified natural gas supplies.

ACKNOWLEDGEMENTS

The research has been supported by the National Research Programme project "Trends, Challenges and Solutions of Latvian Gas Infrastructure Development" (LAGAS) (No. VPP-EM-INFRA-2018/1-0003).

REFERENCES

1. Delliote. (n.d.). *Fit for 55 Package. EU Legislative Action for the Climate*. Available at https://www2.deloitte.com/lv/en/pages/consulting/solutions/Fit-for-55-package.html
2. EC. (2022). *Questions and Answers on the EU Taxonomy Complementary Climate Delegated Act Covering Certain Nuclear and Gas Activities*. Available at https://ec.europa.eu/commission/presscorner/detail/en/QANDA_22_712
3. Savickis, J., Zemite, L., Zeltins, N., Selickis, A., & Ansone, A. (2020). The Biomethane Injection into the Natural Gas Networks: The EU's Gas Synergy Path. *Latvian Journal of Physics and Technical Sciences, 57* (4), 34–50. doi: 10.2478/lpts-2020-0020

4. Savickis, J., Ansone, A., Zemite, L., Bode, I., Jansons, L., Zeltins, N. … & Dzelzitis, E. (2021). The Natural Gas as a Sustainable Fuel Alternative in Latvia. *Latvian Journal of Physics and Technical Sciences, 58* (3), 169–185. doi: https://doi.org/10.2478/lpts-2021-0024
5. Hauser, P., & Most, D. (2015). Impact of LNG imports and shale gas on a European natural gas diversification strategy. In *12th International Conference on the European Energy Market (EEM),* (pp. 1–5), 19–22 May 2015, Lisbon, Portugal.
6. Meza, A., Koc, M., & Saleh Al-Sada, M. (2022). Perspectives and Strategies for LNG Expansion in Qatar: A SWOT Analysis. *Resources Policy, 76*. https://doi.org/10.1016/j.resourpol.2022.102633
7. Najm, R., & Matsumoto, K. (2020). Does Renewable Energy Substitute LNG International Trade in the Energy Transition? *Energy Economics, 92*. https://doi.org/10.1016/j.eneco.2020.104964
8. Euractiv. (2011). *Baltic Countries Ask EU to Solve LNG Terminal Row*. Available at https://www.euractiv.com/section/energy/news/baltic-countries-ask-eu-to-solve-lng-terminal-row/
9. Euractiv (2022). *LEAK: EU Drafts Plan to Ditch Russian Gas*. Available at https://www.euractiv.com/section/energy/news/leak-eu-drafts-plan-to-ditch-russian-gas/
10. Communication from the Commission to the European Parliament, the European Council, the Council, the European economic and social committee and the Committee of the regions. REPowerEU: Joint European Action for more affordable, secure and sustainable energy, COM/2022/108. Final. Available at https://eur-lex.europa.eu/legal-content/EN/TXT/?uri=COM%3A2022%3A108%3AFIN
11. International Energy Agency. (2022). *A 10-Point Plan to Reduce the European Union's Reliance on Russian Natural Gas*. Available at https://iea.blob.core.windows.net/assets/1af70a5f-9059-47b4-a2dd-1b479918f3cb/A10-PointPlantoReducetheEuropeanUnionsRelianceonRussianNaturalGas.pdf
12. ACER. (n.d.). *EU Gas Wholesale Markets 2015-2020*. Available at https://app.powerbi.com/view?r=eyJrIjoiMjJmYWQ4NjctYWIwNC00NzNjLWI5MmMtODVmOTQ0M2Q5YmI4IiwidCI6ImU2MjZkOTBjLTcwYWUtNGRmYy05NmJhLTAyZjE4Y2MwMDA3ZSIsImMiOjl9
13. Trading Economics. (2022). *EU Natural Gas, TTF Gas*. Available at https://tradingeconomics.com/commodity/eu-natural-gas
14. Euractiv. (2022). *Russian Gas Flows via Yamal Pipeline to Germany Decline Sharply*. Available at https://www.euractiv.com/section/global-europe/news/russian-gas-flows-via-yamal-pipeline-to-germany-decline-sharply/
15. France24. (2022). *Russian Gas Supplies to Europe Decline Sharply*. Available at https://www.france24.com/en/tv-shows/business-daily/20220303-russian-natural-gas-supplies-to-europe-decline-yamal-pipeline
16. Energypost. (2022). *Yamal-Europe Gas Pipeline Shows how EU Competition Rules Backfire during a Shortage*. Available at https://energypost.eu/yamal-europe-gas-pipeline-shows-how-eu-competition-rules-backfire-during-a-shortage/
17. Ministry of Economics. (2020). *Latvian Preventive Action Plan for Natural Gas*. Available at https://docplayer.lv/211717165-Latvijas-prevent%C4%ABv%C4%81s-r%C4%ABc%C4%ABbas-pl%C4%81ns-dabasg%C4%81zei.html
18. Ekonomikas ministrija. (2020). *Dabasgāzes apgādes drošums*. Available at https://www.em.gov.lv/lv/dabasgazes-apgades-drosums
19. Conexus. (2022). *Announced an Early Warning in the Natural Gas Supply Sector.* Available at https://www.conexus.lv/aktualitates-sistemas-lietotajiem-eng-575/izsludinats-agrinais-bridinajums-dabasgazes-apgades-nozare

20. Amber Grid. (2022). *Amber Grid Signs Works Contract for Project ELLI in Preparation for Doubling Gas Transmission Capacity between Lithuania and Latvia*. Available at https://www.marketscreener.com/quote/stock/AB-AMBER-GRID-44154872/news/AB-Amber-Grid-Amber-Grid-signs-works-contract-for-project-ELLI-in-preparation-for-doubling-gas-tra-37836684/
21. Esmaeili, M., Shafie-khah, M., & Catalao, J. (2022). A System Dynamics Approach to Study the Long-Term Interaction of the Natural Gas Market and Electricity Market Comprising High Penetration of Renewable Energy Resources. *International Journal of Electrical Power & Energy Systems*, *139*. https://doi.org/10.1016/j.ijepes.2022.108021
22. Borenstein, S., Bushnell, J.B., & Wolak, F. A. (2002). Measuring Market Inefficiencies in California's Restructured Wholesale Electricity Market. *American Economic Review, 92* (5). doi: 10.1257/000282802762024557
23. WoodMakenzie. (2022). *Gas and LNG: Predictions for 2022*. Available at https://www.woodmac.com/news/opinion/gas-and-lng-predictions-for-2022-2022-outlook/
24. Skulte LNG terminal. (n.d.). *The project*. Available at https://www.skultelng.lv/en/the_project/
25. EC. (2022). *Supply, Transformation and Consumption of Gas*. Available at https://ec.europa.eu/eurostat/databrowser/view/NRG_CB_GAS__custom_2274868/default/table?lang=en
26. Booz&Co. (2012). *Analysis of Costs and Benefits of Regional Liquefied Natural Gas Solution in the East Baltic Area, Including Proposal for Location and Technical Options under the Baltic Energy Market Interconnection Plan Final Project Report.* Available at https://energiatalgud.ee/sites/default/files/images_sala/1/16/Booz%26Co_LNG_in_the_East-Baltic_region.pdf
27. Public Utilities Commission. (2022). *Gas Trader List*. Available at https://www.sprk.gov.lv/content/registresanalicencesana
28. Conexus Baltic Grid. (2019). *Medium Term Strategy 2019-2023*. Available at https://www.conexus.lv/uploads/filedir/Media/conexus_mid_term_strategy.pdf
29. Zemite, L., Ansone, A., Jansons, L., Bode, I., Dzelzitis, E., Selickis, A., & Vempere, L. (2021). The Creation of the Integrated Natural Gas Market in the Baltic Region and its Legal Implications. *Latvian Journal of Physics and Technical Sciences, 58* (3), 201–213. DOI: https://doi.org/10.2478/lpts-2021-0026
30. Enerģētikas likums. (1998). Available at https://likumi.lv/ta/id/49833-energetikas-likums
31. Par sabiedrisko pakalpojumu regulatoriem. (2000). Available at https://likumi.lv/ta/id/12483-par-sabiedrisko-pakalpojumu-regulatoriem
32. Directive 2009/73/EC of the European Parliament and of the Council of 13 July 2009 concerning common rules for the internal market in natural gas and repealing Directive 2003/55/EC. Available at https://eur-lex.europa.eu/legal-content/EN/ALL/?uri=celex%3A32009L0073
33. Ruester, S. (2015). *Financing LNG Projects and the Role of Long-Term Sales-and-Purchase Agreements*. Available at https://globallnghub.com/wp-content/uploads/attach_84.pdf
34. Stern, J. (2019). *Challenges to the Future of LNG: Decarbonisation, Affordability and Profitability*. Oxford Institute for Energy Studies. Available at https://www.oxfordenergy.org/wpcms/wp-content/uploads/2019/10/Challenges-to-the-Future-of-LNG-NG-152.pdf
35. NRF. (2018). *LNG Construction Arbitration – From the Beginning to the End*. Available at https://www.nortonrosefulbright.com/en/knowledge/publications/de6861c4/lng-construction-arbitration---from-the-beginning-to-the-end%20
36. PwC. (2014). *The Progression of an LNG Project. Canadian LNG Projects*. Available at https://www.pwc.com/gx/en/mining/publications/assets/pwc-lng-progression-canada.pdf

37. Marine Environment Protection and Management Law (2010). Available at https://likumi.lv/ta/en/en/id/221385
38. Law on Ports. (1994). Available at https://likumi.lv/ta/en/en/id/57435
39. On Environmental Impact Assessment. (1998). Available at https://likumi.lv/ta/en/en/id/51522
40. Construction Law. (2013). Available https://likumi.lv/ta/en/en/id/258572
41. Spatial Development Planning Law. (2011). Available at https://likumi.lv/ta/en/en/id/238807
42. Savickis, J., Zemite, L., Jansons, L., Zeltins, N., Bode, I., Ansone, A., … & Koposovs, A. (2021). Liquefied Natural Gas Infrastructure and Prospects for the Use of LNG in the Baltic States and Finland. *Latvian Journal of Physics and Technical Sciences, 58* (2), 45–64. doi: 10.2478/lpts-2021-0011

LATVIAN JOURNAL OF PHYSICS
AND TECHNICAL SCIENCES
2022, N 2

DOI: 10.2478/lpts-2022-0011

APPLICATION POSSIBILITIES OF THE OFF-GRID HVAC SYSTEM OPERATION SOLUTION FOR TEMPORARY SHELTERS IN THE LATVIAN CLIMATE CONDITIONS

D. Zajecs, K. Lebedeva*, T. Odineca

Riga Technical University,
Department of Heat Engineering and Technology
6 Kipsalas Str., Riga, LV-1048, LATVIA
*e-mail: kristina.lebedeva@rtu.lv

Temporary shelters are extensively used by emergency services (rescue, disaster relief, military response) and other end-users requiring temporary mobile power solutions for different purposes (event organization, vacation homes, summer camps, etc.). The Covid-19 pandemics resulted in an increase of motor homes worldwide sales.

When temporary shelter connection to power grid is impossible, the off-grid liquid fossil fuel generator can be used for electricity generation. Since the liquid fuel supply is often limited, the stock of fuel requires storage that may pose an explosion risk. Quickly installable and energy-efficient ventilation / cooling system with heat recovery is essential to ensure adequate air hygiene and occupants' comfort in temporary structure.

This paper presents a mobile modular electric energy generating unit with photovoltaic (PV) panels for providing temporary shelters (tents) in Latvian climate conditions with heating, ventilation, and air conditioning (HVAC). All calculations were performed using the computer model developed with TRNSYS tool and based on real data from mobile modular energy unit for spring, summer and autumn 2020 and winter 2021. The results show that mobile modular energy unit can be successfully applied for off-grid HVAC system operation of temporary shelters in the Latvian climate conditions.

Keywords: *Emergency energy supply, HVAC, mobile modular energy unit, off-grid, PV, temporary shelters.*

1. INTRODUCTION

By the end of 2019, 79.5 million people, of whom 26.0 million were refugees, had been forcibly displaced due to persecution, conflict, violence, human rights abuses or serious public order [1]. The camps were home to more than 6.6 million refugees and people in refugee-like situations, of whom 4.6 million were in planned / managed camps and about 2 million in self-employed camps [2]. Indoor comfort and HVAC systems efficiency were often ignored in the temporary shelter design process, as they were primarily built to provide safety of camp residents. Studies [3], [4] show that such camps are mostly concentrated in regions with a harsh, often extremely hot climate, and the indoor temperature in shelters can reach 39–46 °C. These data show the need to maintain an appropriate microclimate in temporary shelters. The indoor air quality is essential not only for residential but also for military personnel despite their relatively better physical conditions [6], [7]. Most of the operational energy demand in temporary off-grid structures is accounted for HVAC requirements. During periods of extreme weather conditions, HVAC systems consume up to 60 % of the fossil liquid fuel (diesel) allocated to military forward operating bases [5].

The temporary camps of military bases, disaster relief sites, temporary search, rescue or recreation camps are most often located in areas distant from the power grid. The deployable tents, easy to transport and mount, are most often used as premises. The living indoor comfort conditions of such premises entirely depend on weather. The reality is that disasters, whether human or natural, tend to be unique in terms of shelter budget, availability of materials, etc. which makes it nearly impossible to plan ahead the grid connection of the shelters [8], constant supply of liquid fossil fuel, as well as safe fuel storage conditions.

One of the possible solutions to generate electricity autonomously is the use of off-grid mobile PV system, such as Zerobase Energy's T-Series system mobile – towable trailer with PV panels and storage battery, and solar PV and hybrid (wind and/or portable generator) input [9]. One more example is a mobile PV-Wind-Battery-Diesel Hybrid System unit, constructed inside a transportable container [10]. The authors [9], [10] proposed that a new generation of mobile solar PV solutions should be more affordable to the community and easier in use.

This paper presents a mobile modular energy generating unit with PV system for the HVAC system operation in temporary shelters.

The unit provides simultaneous supply of electricity, heating and cooling and has a built-in heat recovery device. This quickly installable and energy-efficient ventilation system is essential to ensure adequate air hygiene and occupants' comfort in temporary structures. The developed working prototype (Fig. 1) is assembled on a common car trailer base and can be towed by a light vehicle. The estimated size of the trailer is the following: width 1.8 m, length 3.7 m, height 1.6 m.

a) operation condition

b) transportation condition

Fig. 1. Mobile modular energy unit.

2. MATERIALS AND METHODS

The developed mobile modular energy unit includes eight photovoltaic cells for power generation. The electricity is converted into thermal energy in the heat supply unit and/or is directly supplied to the consumers. When energy is not consumed, it is stored in the energy storage battery. If necessary, it is possible to start a diesel generator. In order to extend the autonomous life of the mobile modular energy unit and to increase the overall efficiency of the system, heat recovery unit is provided. Heat recovery is an essential part of modern energy efficient HVAC [11]. Unit cooling capacity is ≥8 kW, and heating capacity ≥9 kW. The heat is produced using a highly efficient air / air heat pump compression cycle, which can also provide the consumer with cooling demand. Heat pumps are proved as an energy efficient solution both in hot and cold climate conditions [12], [13] . The control of the mobile modular energy unit is implemented by means of an energy management unit, which is connected to the Internet enabling a remote control. The principal scheme and technical characteristics of the proposed mobile modular energy unit are shown in Fig. 2 and Table 1.

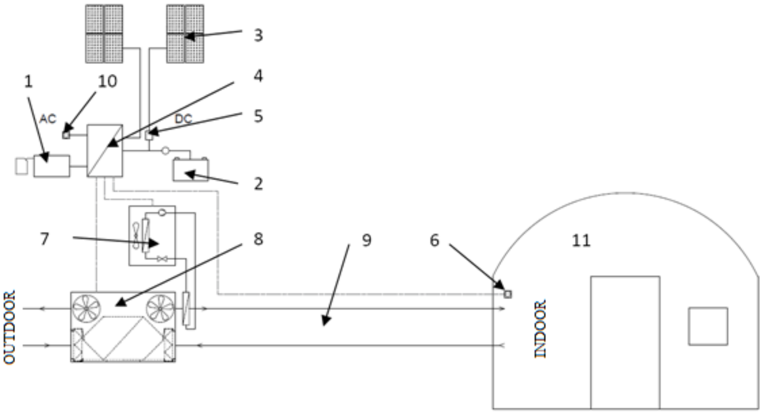

1 – diesel generator; 2 – battery; 3 – PV panels; 4 – inverter; 5 – controller; 6 – consumers' power connector; 7 – heat pump; 8 – air-to-air heat recovery device; 9 – air supply / exhaust channels; 10 – connection to the power supply; 11 – shelter.

Fig. 2. The principal scheme of the mobile modular energy unit.

Table 1. Technical Characteristics of the Mobile Modular Energy Unit

PV Power (Wp)	2400
Inverter Power (W)	Cont. output power at 25 °C = 3000VA / 2400W
Batteries (N - V - Ah)	2 batteries provide: Rated voltage 12.8V Nominal capacity at 25 °C 200 Ah Nominal capacity at 0 °C 160 Ah Nominal capacity at -20 °C 100 Ah Number of cycles at 80 % charge: 2500
Battery Capacity (Wh)	Rated energy at 25 °C 2560 Wh
Dimensions Closed (m)	1.8 x 3.7 x 1.6
Dimensions Opened (m)	4.4 x 3.7 x 1.6
Weight (Kg)	1350

Based on the research carried out by the Department of Heat Engineering and Technology of Riga Technical University [14], it was decided to evaluate the ability of the mobile modular energy unit system to meet the temporary tent need for HVAC operation systems in the climate conditions of Riga, Latvia. All calculations were performed using a computer model (Fig. 3) developed for this purpose with the help of the transient system simulation (TRNSYS) software tool. TRNSYS was chosen because of its extensive component library and simulation capabilities, especially in the field of renewable energy. Its capability was demonstrated in studies [15] (modelling the performance of a solar photovoltaic thermal collector (PVT)) and [16] (simulation of energy systems with PV; for cold climate adding the PVT, floor heating, and a generator for increasing the heat load). The model validation was based on the real modular energy unit operation data. The necessary data were obtained by the energy management software from the sensors installed inside the tent.

The input data for energy simulation are shown in Table 2. Depending on the air temperature in the tent and the desired air temperature according to timetable shown in Table 2, the differential controllers send on/off signals to the heat pump and to the air-to-air heat recovery device. The parameters of a tent in TRNSYS were adopted according to the parameters of the manufacturer's specification (5 m x 4 m x 2.3 m). The U – heat transfer coefficient of a PVC coated fabric [17] is shown in Table 2.

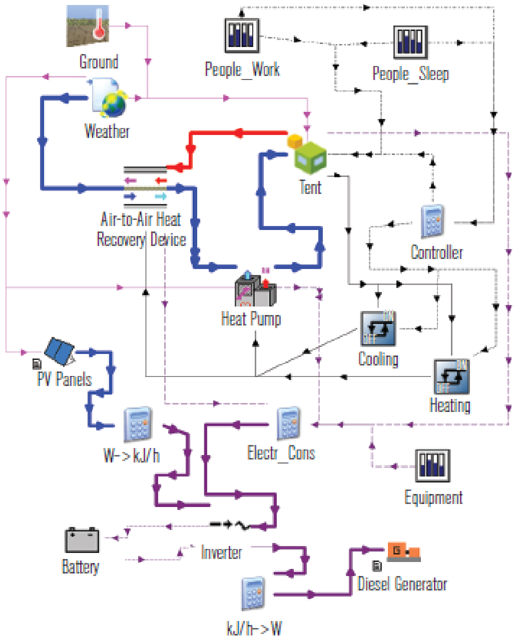

Fig. 3. Computer model.

Table 2. Input Data for Energy Simulation

The input data of tent	
Parameters	**Value**
Roof and wall	U=1.13 W/m^{2}K
Floor	U=0.87 W/m^{2}K
Volume	35.25 m^3
Area	20 m^2 floor; 48.6 m^2 walls and roof
Heat Loss	73.32 W/K
Capacitance	42.3 kJ/K
Weather	Riga, Latvia
Timetable	

Time	**Occupant**		**Heating Temperature (°C)**	**Cooling tempera-ture (°C)**	**Light (W)**	**Equip-ment (W)**
	Count	**W (met)**				
12 AM–6 AM	5	100 (0.9)	18 ± 2	23 ± 1	-	-
6 AM–10 AM	2	125 (1.1)	18 ± 2	23 ± 1	55	-
10 AM–1 PM	0	-	5 ± 2	27 ± 1	-	-
1 PM–3 PM	5	125 (1.1)	18 ± 2	23 ± 1	55	300
3 PM–8 PM	0	-	5 ± 2	27 ± 1	-	-
8 PM–10 PM	5	125 (1.1)	18 ± 2	23 ± 1	55	40
10 PM–12 AM	5	100 (0.9)	18 ± 2	23 ± 1	-	-

Table 3. Mobile Modular Energy Unit Parameters

Parameter	**Value**	**Parameter**	**Value**
PV Panels		**Battery**	
Azimuth of surface, slope of panel	South, 0^0	Cell energy capacity	200 Ah
Power	400 Wp	Cells	8
Voltage at max Power point	33.21 V	Charging efficiency	0.92
Current at max Power point	9.23 A	Max charge voltage per cell	2.8 V
Module area	1.46 m^2	**Inverter**	
Number of modules	6	Regulatory efficiency	0.98
Heat Pump		Inverter efficiency	0.94
-20 °C outside DBT*	Heating capacity 3.52 kW	High limit on FSOC **	100 %
5 °C intake DBT	Heating power 1.76 kW	Charge to discharge limit on FSOC	0 %
29 °C outside DBT	Cooling capacity 3.50 kW	Inverter output power capacity	2400 W
22 °C intake DBT	Cooling Power 0.95 kW	Upper limit on FSOC for grid charging	100 %
Air-to-air heat recovery device		Current for grid charging of battery	100 A
Heat recovery sensible effectiveness	0.797	**Diesel generator**	
Heat recovery latent effectiveness	0.889	Rated power	2.0 kW
Ventilation flow rate	350 m^3/h	Max power	2.4 kW
Ventilation fan total power	150 W	Min power	0.6 kW

* dry-bulb temperature

** fractional state of charge

It was assumed that the model would take into account heat production from human and lighting and the electricity consumption of equipment (see Table 2). The maximum possible electrical load was approximately 2.3 kW. There was no air recirculation inside the shelter and ventilation was provided only while heating. As the simulation results showed, the supply air (at an airflow rate of 350 m^3/h) needed to be cooled to a comfortable temperature by 10–15 degrees in summer. In winter, the supply air was heated 30–35 degrees above the outdoor temperature. The heat pump power was set 15 degrees above indoor / outdoor temperature difference. While operating in winter mode, the diesel generator was connected to provide a system with additional electricity.

The components and parametrs of mobile modular energy unit are presented in Table 3.

3. RESULTS AND DISCUSSION

Simulations were made for one-year period (four seasons), for Riga, in the Latvian climate conditions, using both climatic databases and the operational real data of the mobile modular energy unit. Table 4 presents real operation data of the mobile modular energy unit.

Table 4. Operational Data of Mobile Modular Energy Unit

	Winter	Spring	Summer	Autumn
Electricity consumed (kWh)	1,001	4,22	5,20	354
Diesel generator produced electricity (kWh)	1,173	210	60	370
Diesel consumed (l)	378	70	20	119
Diesel generator work time (h)	955	193	55	298

Approximately 60 % of the heat supplied from the exhaust air in winter, in spring and autumn is recovered by an air-to-air heat recovery device.

The maximum diesel fuel consumption is in the winter period. During other seasons, (in most cases) the PV produced electricity is greater than the amount of electricity consumed by a HVAC system per day.

Table 5. Statistical Results

		Electricity consumption per day, kWh	Difference, % (PV produced electricity/electricity consumed per day)	Airflow of occupied shelter, kg/h	Diesel fuel consumption, l/day
Winter	Min	4.23	1	103	1.43
	Max	27.25	81	352	8.17
	Mean	11.12	16	173	4.20
	SD*	4.93	17	50	1.37
Spring	Min	1.31	16	4	0.00
	Max	12.34	741	168	4.16
	Mean	4.59	269	75	0.76
	SD	2.53	203	44	1.01
Summer	Min	1.12	8	4	0.00
	Max	9.50	962	118	2.20
	Mean	3.15	320	53	0.30
	SD	1.88	180	36	0.98
Autumn	Min	1.29	3	3	0.00
	Max	13.44	474	171	5.07
	Mean	3.89	128	65	1.31
	SD	2.46	131	40	1.40

* standard deviation

Table 5 presents one-year simulations based on real energy data statistical results of electricity consumption/production of the mobile modular energy unit. For simulations, it was assumed that the airflow was 4.0 l/s per person [18]. Taking into account that the Latvian construction standards neither determine the required minimum amount of ventilation air, nor provide indications of the values that should be adopted, the regulations of other countries were applied.

Simulations showed that the airflow of the occupied shelter was 4.8–16.3 l/s per person in winter and 0.2–7.8 l/s per person during other seasons. For this type of shelters (tent), the airflow rate strictly depends on the outside temperature. In summer, the system mostly operated without a diesel generator because electricity generated by PV and stored in batteries was completely sufficient to provide HVAC system operation.

To demonstrate the PV panel impact, the simulations without PV were performed only for off-grid operation of the shelter using the diesel generator (Table 6).

Table 6. PV panel Impact

		Produced electricity, kWh	Diesel fuel consumption, l		Diesel generator work time, h	
Winter	Without PV	0	416	-	1,054	-
	PV	132	378	-9 %	955	-9 %
Spring	Without PV	0	241	-	632	-
	PV	797	70	-71 %	193	-69 %
Summer	Without PV	0	300	-	792	-
	PV	1203	20	-93 %	55	-93 %
Autumn	Without PV	0	205	-	506	-
	PV	286	119	-42 %	298	-41 %

According to Table 6, it can be concluded that for the mobile modular energy unit with PV panels, which put in action the HVAC system, the diesel generator would reduce diesel fuel consumption to 71–93 % in the spring and summer period and to 9 % in winter in the Latvian climate conditions. These are very good indicators, considering that, when the energy unit operates using PV, only 20 l of diesel fuel are needed during the whole summer season.

4. CONCLUSIONS

Comparing the amount of energy required for the HVAC system of the shelter, the modular energy unit can provide autonomous work by 50 % during the year while operating only the PV panels, without the fossil fuel generator. If we accept that temporary shelters operate only in the summer season, the modular energy unit can provide autonomous work by 93 %. Table 7 presents simulation data for cities with similar climate conditions.

Table 7. Summary of Annual Operation of Mobile Energy Unit

Town	Electricity, kWh			Energy, kWh			Time, h		
	Total required	PV produced	Additional required	Heat recovered	Heat supplied	Cool supplied	Heating	Cooling	Diesel work
Stockholm	1968	2313	1639	5585	3669	392	1626	115	1369
Riga	1989	2268	1674	5571	3616	457	1600	134	1460
London	944	2169	577	1895	1152	559	609	165	412

The amount of electricity generated annually by the PV panels of the mobile energy unit is higher than the demand. Therefore, the optimal heating and cooling algorithms for different applications should be further explored – different types of shelters, their sizes, thermal properties, equipment load and planning, required internal temperature and airflow rate depending on different seasons. Additionally, the real operation data received within only one year is insufficient for creation of a reliable computer model. For better model validation, the second year of data processing of the mobile energy unit use in real conditions has already begun.

ACKNOWLEDGEMENTS

The research has been supported by Doctoral Grant programme DOK.BIF/20 of Riga Technical University and European Regional Development Fund project No. 1.1.1.1/16/A/048 "Nearly Zero Energy Solutions for Unclassified Buildings".

REFERENCES

1. UNHCR. (2020). *Trends at a Glance: Global Trends Forced Displacement in 2019*. Available at https://www.unhcr.org/flagship-reports/globaltrends/globaltrends2019/#:~:text=One%20per%20cent%20of%20the,to%20outpace%20global%20population%20growth.&text=During%202019%2C%20an%20estimated%2011.0%20million%20people%20were%20newly%20displaced
2. UNHCR. (2021). *Shelter*. Available at https://www.unhcr.org/uk/shelter.html
3. Fosas, D., Moran, F., Natarajan, S., Orr, J., & Coley, D. (2020). The Importance of Thermal Modelling and Prototyping in Shelter Design. *Building Research and Information*, *48* (4). doi: 10.1080/09613218.2019.1691489.
4. Albadra, D., Coley, D., & Hart, J. (2018). Toward Healthy Housing for the Displaced. *The Journal of Architecture*, *23* (1). doi: 10.1080/13602365.2018.1424227.
5. Lee, D.S., Iacocca, M., & Joshi, Y.K. (2021). Energy Usage Modeling for Heating and Cooling of Off-grid Shelters. *Journal of Building Engineering*, *35*. doi: 10.1016/j.jobe.2020.102054.
6. White, D.W., Feigley, C.E., McKeown, R.E., Hout, J.J., & Hebert, J.R. (2011). Association between Barracks Type and Acute Respiratory Infection in a Gender Integrated Army Basic Combat Training Population. *Military Medicine*, *176* (8). doi: 10.7205/MILMED-D-10-00418.

7. Prozuments, A., Borodinecs, A., & Zemitis, J. (2020). Survey Based Evaluation of Indoor Environment in an Administrative Military Facility. *Journal of Sustainable Architecture and Civil Engineering*, *27* (2). doi: 10.5755/j01.sace.26.2.26079.
8. Moran, F., Fosas, D., Coley, D., Natarajan, S., Orr, J., & Ahmad, O.B. (2021). Improving Thermal Comfort in Refugee Shelters in Desert Environments. *Energy for Sustainable Development*, *61*. doi: 10.1016/j.esd.2020.12.008.
9. Franceschi, J., Rothkop, J., & Miller, G. (2014). Off-grid Solar PV Power for Humanitarian Action: From Emergency Communications to Refugee Camp Micro-Grids. *Procedia Engineering*, *78*. doi: 10.1016/j.proeng.2014.07.061.
10. Prompinit, K., Plangklang, B., & Hiranvarodom, S. (2011). Design and Construction of a Mobile PV Hybrid System Prototype for Isolated Electrification. *Procedia Engineering*, *8*. doi: 10.1016/j.proeng.2011.03.025.
11. Borodinecs, A., Prozuments, A., Zajacs, A., & Zemitis, J. (2019). Retrofitting of Fire Stations in Cold Climate Regions. *Magazine of Civil Engineering*, *90* (6). doi: 10.18720/MCE.90.8.
12. Jaundalders, S., Stanka, P., & Rusovs, D. (2017). Seasonal Performance for Heat Pump with Vertical Ground Heat Exchanger in Riga. *IOP Conference Series: Materials Science and Engineering*, *251* (1). doi: 10.1088/1757-899X/251/1/012057.
13. Bogdanovičs, R., Borodinecs, A., Zajacs, A., & Šteinerte, K. (2018). Review of Heat Pumps Application Potential in Cold Climate. *Advances in Intelligent Systems and Computing, 692*, 543. doi: 10.1007/978-3-319-70987-1_58.
14. Bogdanovics, R., Borodinecs, A., Zemitis, J., & Zajacs, A. (2021). Using a Mobile Modular Energy Unit with PV Panels for Heating. *ASHRAE Journal*, *63* (4), 38–46.
15. Khordehgah, N., Guichet, V., Lester, S.P., & Jouhara, H. (2019). Computational Study and Experimental Validation of a Solar Photovoltaics and Thermal Technology. *Renewable Energy*, *143* (C), 1348–1356. doi: 10.1016/j.renene.2019.05.108.
16. Kristiansen, A.B., Zhao, B.Y., Ma, T., & Wang, R.Z. (2021). The Viability of Solar Photovoltaic Powered Off-grid Zero Energy Buildings Based on a Container Home. *Journal of Cleaner Production*, *286*. doi: 10.1016/j.jclepro.2020.125312.
17. Outdoor Venture Corporation. (n.d.). *Military Shelters and Accessories*. Available at https://outdoorventure.com/our-products/military-shelters-and-accessories/temper/temper-tent-module
18. ASHRAE (2010). *ASHRAE Standard 62.1-2010. Ventilation for Acceptable Indoor Air Quality.* Available at http://arco-hvac.ir/wp-content/uploads/2016/04/ASHRAE-62_1-2010.pdf

LATVIAN JOURNAL OF PHYSICS
AND TECHNICAL SCIENCES
2022, N 2

DOI: 10.2478/lpts-2022-0012

STUDY ON MASS AND LINEAR ATTENUATION COEFFICIENTS OF PMMA AS HUMAN TISSUE-EQUIVALENT MATERIAL

M. S. Hamideen[1]*, Abady R.S[2], J.M. Sharaf[3]

[1]Department of Physics and Basic Sciences,
Faculty of Engineering Technology,
Al-Balqa Applied University, P.O. Box 2587, Amman, 11941, JORDAN
[2]Department of Physics, Faculty of Science, Al-Balqa Applied University,
P.O. Box 2587, Amman, 11941, JORDAN
[3]Department of Physics, the University of Jordan,
P.O. Box 13535, Amman, 11941, JORDAN
*e-mail: mhamideen@bau.edu.jo

To research the improvements of clinical imaging of human tissues, tissue-equivalent materials are one of the reasonable strategies for evaluating the impact of radiation dosages on human tissues. Hence, considering mass and linear attenuation coefficients is a promising method to foresee the appropriate tissue-identical material. In this examination, we utilise the built-up estimations of elemental compositions (mass portion of every component) of PMMA material by numerous analyses in literature. XCOM program was utilised to figure estimations of mass attenuation coefficients of PMMA for various photon energies (0.015–2.0) MeV. The outcomes reveal that the estimations of mass and linear attenuation coefficients are high as the energies begin to decrease and diminish gradually with an expansion in photon energies. Making a sensible coordinating between mass and linear attenuation coefficients of PMMA as human tissue-equivalent material with mass and linear attenuation coefficients of lung, brain, muscle and blood human tissues has demonstrated a phenomenal match.

Keywords**:** *Human organs and tissues, linear attenuation coefficient, mass attenuation coefficient, tissue-equivalent materials.*

1. INTRODUCTION

Cancer treatment techniques, these days, are generally presented, for example, in chemotherapy, radiotherapy, brachytherapy and medical procedure [1]. The reason for brachytherapy is to put radioactive sources into the influenced part with an expanded portion, while the normal tissues get a limited portion of radiation. A fruitful brachytherapy treatment arranging measure needs to limit the progressions between the assessed and conveyed dosages [2], [3]. Numerous perspectives make this intrigue hard to show up at, for example, the quick decaying of dose close to tumour, mistakes in the techniques used to ascertain the dose and errors in assessment of the dose variety in heterogeneous regions. In spite of these aspects, significant accomplishments have been reached in the late decades because of accessibility of weak ^{137}Cs and strong ^{192}Ir sources of various plans notwithstanding the foundation of quality control techniques that can administer the exactness of the planned strategy. These days, numerous ways have been actualized to test the dose consumed close to sources by utilising the information base and reasonable phantoms. The phantoms, built in order to adjust to quality control norms, are produced using tissue-equivalent materials to simulate human tissues to be irradiated. From the clinical physical science perspective, human tissue-equivalent materials give a few issues in mimicking the human tissues in low and high energy ranges [4]. In many contemplated works, the dose conveyance in numerous human tissue substitutes was determined. Dose appropriations in water and delicate tissue apparitions and dosimetric boundaries of a ^{131}Cs source, utilising a Monte Carlo study have been determined [5]. It has been discovered that Polyethylene, Polystyrene, Perspex, and Nylon well reproduce fat and muscle, Plaster of Paris well mimics cortical bone, Polypropylene well mimics fat tissues and yellow bone marrow tissues, polycarbonate well mimics spongiosa. Specialists worked to decide on the portion brought about by the presence of in-homogeneities, in water phantoms, utilising ^{192}Ir source and Monte Carlo recreation code [6]. Dose circulations near ^{192}Ir source in various human tissue-comparable materials utilising three Monte Carlo codes have been concentrated by another gathering of specialists [7]. The discoveries of the last examinations investigated that radial dose functions were influenced in bone tissue and inferred that clinical aspects did not give enough exact dose assurance for some materials. These materials were compared with the reference materials found in report no. 44 of ICRU [8]. Further, to develop monetarily appropriate human tissue substitutes for phantom fabricate, atomic numbers and electron densities were resolved reliant on mass attenuation coefficient values. Fadhil et al. (2017) chose the elemental compositions and attenuation properties of gelatin for utilising it as a test materials to assess the impact of ionizing radiation on tissues [9]. Kurudirek and Özdemir (2011) tried the legitimacy of utilising tissue proportionate materials for dosimetric estimations [10].

In this work, a methodology is created to research scatter and absorption properties of PMMA as a human tissue-proportional material. The interaction of photon with tissues is inspected fundamentally to the extent tissue attenuation coefficients inside the energy range utilised in brachytherapy (0.15–2.0 MeV). The linear attenuation coefficient (μ) is the probability of collaboration of photons per unit separation in an engaging medium. The mass attenuation coefficient is a proportion of the average number of interactions that happen in a given mass-per-unit area of tissue [11]. The mass attenuation coefficient, μ_m ($\mu_m=\mu/\rho$) is of more vital importance than μ, it does not depend on the thickness and physical condition of the medium, it plays as a significant coefficient, since simply the atomic arrangement of the attenuator is considered and not its individual density. It is a proportion of material ability to ingest or dissipate radiation per unit of mass [12]. Then again tissue equivalent atomic number (Z_{eq}) is a noteworthy limit in anticipating and surveying the transport of photon progress in tissue and checking the radiation partition devoured by it. On the other hand, tissue equivalent atomic number (Z_{eq}) is a basic cutoff in foreseeing and reviewing the transport of photon flux in the irradiated tissue and consumed dose rate assessment. Scattering and absorption properties of a single element are identified with its thickness and atomic number, while for a composite material it is identified with its effective thickness and equivalent atomic number. The point of this examination is to drive and process photon interaction boundaries, for PMMA as a human tissue substitute, so as to apply the ideas of photon collaborations and dosimetry and to propose a valuable system ready to explore material tissue equivalence.

2. METHODOLOGY

The linear attenuation coefficient μ is the most noteworthy variable to depict the association between radiation entrance and absorption material along its way for each unit distance inside this tissue. It relies upon the atomic number of the material and the energy of the radiation. Taking into account Hubbell and Seltzer's (1997) speculation, the mass attenuation coefficient (μ/ρ) is the entire cross-section of the individual impact values for Rayleigh (σ_R), photoelectric impact (σ_τ), pair creation (κ) and Compton scattering (σ_c) divided by the atomic mass unit (m_u) having the estimation of 1.660 5402 × 10^{-24} g and the relative atomic mass of the absorber (A) as found in the next expression [13]:

$$\mu_m = \frac{\mu}{\rho} = \frac{\sigma_R + \sigma_C + \sigma_\tau + K}{m_u A}.$$

To choose the appropriate tissue-equivalent material, the delayed consequences of mass attenuation coefficient is contrasted with that given in the ICRU no. 44 [8]. This report gives nuances of basic arrangements, mass densities, electron densities and interaction information of all tissues. XCOM photon cross-section information base, which is built up by the National Institute of Standards and Technology (NIST) in light of Hubbell and Seltzer tables, is the most helpful programming in mass attenuation coefficient estimations for some researchers [13],[14]. The last referenced programming is utilised in this work to figure the mass attenuation coefficient after inserting the values of the elemental composition taken from the literature [8], [9], [15], and [16]. Elemental composition (%) (weight part of tissue sections) of picked human tissue examples are presented in Table 1 and the same compositions for PMMA as a human tissue substitute are recorded in Table 2.

Table 1. Elemental Composition (%) of Some Human Tissues [8], [15]

Element	Adipose ρ= 0.92 g cm^{-3}	Skin ρ= 1.10 g cm^{-3}	Muscle ρ= 1.04 g cm^{-3}	Brain ρ=1.03 g cm^{-3}	Blood ρ= 1.06 g cm^{-3}	Lung ρ= 1.05 g cm^{-3}	Soft ρ= 1.00 g cm^{-3}	Bone (compact) ρ= 1.85 g cm^{-3}	Bone (cortical) ρ= 1.85 g cm^{-3}
H	1.19E+01	1.00E+01	1.02E+01	1.11E+01	1.02 E+01	1.01 E+01	1.04 E+01	6.39E+00	4.72E+00
C	6.37E+01	2.28E+01	1.23E+01	1.25E+01	1.00E+01	1.02E+01	2.32E+01	2.78E+01	1.44E+01
N	7.97E-01	4.64E+00	3.50E+00	1.32E+00	2.96E+00	2.86E+00	2.48E+00	2.70E+00	4.19E+00
O	2.32E+01	6.19E+01	7.29E+01	7.37E+01	7.59E+01	7.57E+01	6.30E+01	4.10E+01	4.46E+01
Na	5.00E-02	7.00E-03	8.00E-02	1.84E-01	1.85E-01	1.84E-01	1.13E-01	0.00E+00	0.00E+00
Mg	2.00E-03	6.00E-03	2.00E-02	1.5E-02	4.00E-03	7.30E-02	1.30E-02	2.00E-01	2.20E-01
Si	0.00E+00	0.00E+00	0.00E+00	0.00E+00	3.00E-03	0.00E+00	0.00E+00	0.00E+00	0.00E+00
P	1.60E-02	3.30E-02	2.00E-01	3.54E-01	3.50E-02	8.00E-02	1.33E-01	7.00E+00	1.05E+01
S	7.30E-02	1.59E-01	5.00E-01	1.77E-01	1.85E-01	2.25E-01	1.99E-01	2.00E-01	3.15E-01
Cl	1.19E-01	2.67E-01	0.00E+00	2.36E-01	2.78E-01	2.66E-01	1.34E-01	0.00E+00	0.00E+00
K	3.20E-02	8.50E-02	3.00E-01	3.10E-01	1.63E-01	1.94E-01	1.99E-01	0.00E+00	0.00E+00
Ca	2.00E-03	1.50E-02	0.00E+00	9.00E-03	6.00E-03	9.00E-03	2.30E-02	1.47E+01	2.10E+01
Fe	2.00E-03	1.00E-03	0.00E+00	5.00E-03	4.60E-02	3.7E-02	5.00E-03	0.00E+00	0.00E+00
Zn	2.00E-03	1.00E-02	0.00E+00	1.00E-03	1.00E-02	1.00E-02	3.00E-03	0.00E+00	1.00E-02

Table 2. Elemental Composition (%) of PMMA as Human Tissue-Equivalent Material [9], [16]

Element	H	C	N	O	S
PMMA ρ=1.178 g cm^{-3}	2.40E-03	9.49E-01	4.71E-02	0.00E+00	1.00E-03

3. RESULTS AND DISCUSSION

3.1. Mass Attenuation Coefficients

Tissue-comparable materials are valuable for mimicking human tissues for photon interactions inside the determined energy regions. These materials should hold and disperse radiation comparably, inside commendable cutoff points, as illuminated human tissue. As far as possible, as suggested by the ICRU report no. 44, the precision for dose conveyance in radiotherapy methods should be inside ± 5 %. Materials having great tissue identicalness, normally utilized for apparition reproduction, ought to end up being appropriate in testing dosages for brachytherapy applications. Tissue-comparability of material portrays its ability to collaborate with radiation as genuine tissues did. The mass attenuation coefficient (μ_m) is a basic boundary for photon interactions with the material. It is an extent of the normal number of interactions between scene photons and matter occurring in a given mass-per-unit area of the material experienced. The calculated estimations of μ_m as a function of photon energy, for human tissues and PMMA as a human tissue substitute, is presented in Table 3.

Table 3. Variation of Mass Attenuation Coefficient for Human Tissues and PMMA for Photon Energies (0.015–2.0) MeV

Energy (MeV)	adipose	Skin	Muscle	Brain	Blood	Lung	Soft	Bone compact	Bone cortical	PMMA
0.015	9.44E-01	1.40E+00	1.57E+00	1.59E+00	1.58E+00	1.59E+00	1.43E+00	6.12E+00	8.38E+00	7.42E-01
0.02	4.86E-01	6.66E-01	7.37E-01	7.47E-01	7.41E-01	7.46E-01	6.80E-01	2.70E+00	3.66E+00	3.91E-01
0.03	2.68E-01	3.13E-01	3.33E-01	3.37E-01	3.34E-01	3.36E-01	3.18E-01	9.10E-01	1.19E+00	2.27E-01
0.04	2.17E-01	2.33E-01	2.41E-01	2.43E-01	2.41E-01	2.42E-01	2.35E-01	4.76E-01	5.90E-01	1.89E-01
0.05	1.98E-01	2.04E-01	2.08E-01	2.09E-01	2.08E-01	2.08E-01	2.05E-01	3.22E-01	3.77E-01	1.74E-01
0.06	1.88E-01	1.89E-01	1.91E-01	1.93E-01	1.91E-01	1.91E-01	1.90E-01	2.53E-01	2.83E-01	1.66E-01
0.08	1.75E-01	1.73E-01	1.74E-01	1.76E-01	1.74E-01	1.74E-01	1.74E-01	1.95E-01	2.06E-01	1.56E-01
0.1104	1.62E-01	1.59E-01	1.60E-01	1.61E-01	1.60E-01	1.60E-01	1.60E-01	1.64E-01	1.66E-01	1.45E-01
0.15	1.49E-01	1.47E-01	1.47E-01	1.48E-01	1.47E-01	1.47E-01	1.47E-01	1.45E-01	1.44E-01	1.33E-01
0.2	1.37E-01	1.34E-01	1.34E-01	1.36E-01	1.34E-01	1.34E-01	1.35E-01	1.31E-01	1.29E-01	1.22E-01
0.3	1.19E-01	1.17E-01	1.17E-01	1.18E-01	1.17E-01	1.17E-01	1.17E-01	1.13E-01	1.11E-01	1.07E-01
0.35	1.12E-01	1.10E-01	1.10E-01	1.11E-01	1.10E-01	1.10E-01	1.11E-01	1.07E-01	1.05E-01	1.01E-01
0.5	9.73E-02	9.57E-02	9.58E-02	9.65E-02	9.58E-02	9.57E-02	9.60E-02	9.24E-02	9.09E-02	8.72E-02
0.613	8.91E-02	8.77E-02	8.78E-02	8.84E-02	8.78E-02	8.77E-02	8.80E-02	8.46E-02	8.32E-02	7.99E-02
0.6616	8.62E-02	8.48E-02	8.49E-02	8.55E-02	8.49E-02	8.48E-02	8.51E-02	8.18E-02	8.05E-02	7.73E-02
1.173	6.57E-02	6.46E-02	6.47E-02	6.52E-02	6.47E-02	6.46E-02	6.48E-02	6.24E-02	6.13E-02	5.89E-02
1.2529	6.35E-02	6.25E-02	6.26E-02	6.30E-02	6.25E-02	6.25E-02	6.27E-02	6.03E-02	5.93E-02	5.69E-02
1.3325	6.15E-02	6.05E-02	6.06E-02	6.11E-02	6.06E-02	6.06E-02	6.07E-02	5.84E-02	5.75E-02	5.52E-02
1.33782	6.05E-02	6.04E-02	6.05E-02	6.09E-02	5.95E-02	6.04E-02	6.06E-02	5.83E-02	5.74E-02	5.51E-02
1.5	5.79E-02	5.69E-02	5.70E-02	5.74E-02	5.70E-02	5.70E-02	5.71E-02	5.50E-02	5.41E-02	5.19E-02
1.6	5.59E-02	5.50E-02	5.51E-02	5.55E-02	5.51E-02	5.51E-02	5.52E-02	5.32E-02	5.23E-02	5.02E-02
1.7	5.42E-02	5.33E-02	5.34E-02	5.38E-02	5.34E-02	5.34E-02	5.35E-02	5.15E-02	5.07E-02	4.86E-02
1.8	5.25E-02	5.17E-02	5.18E-02	5.22E-02	5.18E-02	5.18E-02	5.19E-02	5.00E-02	4.92E-02	4.71E-02
1.9	5.10E-02	5.03E-02	5.03E-02	5.07E-02	5.03E-02	5.03E-02	5.04E-02	4.86E-02	4.79E-02	4.58E-02
2.0	4.96E-02	4.89E-02	4.90E-02	4.93E-02	4.89E-02	4.89E-02	4.90E-02	4.73E-02	4.66E-02	4.45E-02

As can be seen from the information recorded in the table, except for bone tissues, the estimations of 7 human tissues and tissue-equivalent material are near one another for a similar photon energy and the contrast between them exists in the range of 0.0 % – 7.0 %. The outcomes are likewise plotted in Fig. 1 for photon energy region between 0.015 and 2.0 MeV. It very well may be seen in the figures that the estimations of all materials decline quickly with photon energy up to about 0.5 MeV, then the qualities decline gradually up to 2 MeV. This variation is because of the variety of partial photon interaction cross-sections.

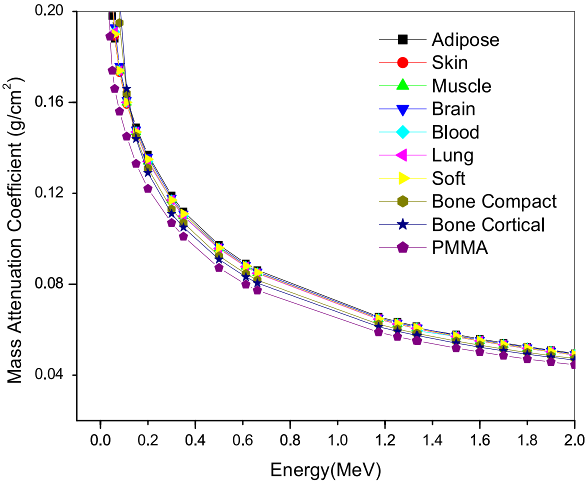

Fig. 1. Variation of mass attenuation coefficient of human tissues and PMMA for photon energies (0.015-2.0) MeV.

However, μ_m values decrease rapidly with photon energy until the photon energy outperforms the binding energy of the electrons and Compton scattering turns into the prevalent interaction. In the Compton range of energies, μ_m value of different materials does not change in a huge amount, since it is autonomous of atomic number Z_{eq}. It follows that the contribution of Compton scattering to μ_m is independent of Z_{eq} but depends only on the material electron density (number of electrons per unit volume), which is almost the same for all materials except hydrogen. The mass attenuation coefficient continues lessening with energy until pair production begins to get possible. The quality of pair production occurs at energies significantly more noticeable than the edge of energy of 1.02 MeV, which is out of our interest in the energy range used in brachytherapy. At last, it should be noticed that qualities will be utilised to drive different photon interaction boundaries, for example, linear attenuation coefficient, which will encourage correlation of radio-physical properties of the chosen tissue-equivalent material (PMMA) with the relating human tissues.

3.2. Linear Attenuation Coefficients

Linear attenuation coefficient (μ) is a helpful boundary for assessing the usage of tissue proportionate materials in dosimetric applications. It is the fundamental boundary required in deciding photon transmission in issue. Computed values of (μ) for the chosen human tissue and PMMA as a human tissue substitute, for the photon energy range of 0.015 to 2 MeV are arranged in Table 4. Estimation of linear attenuation coefficients relies upon the photon energy, chemical composition and, to some extent, electron density or physical density of the investigated materials. The energy reliance of μ values is shown in Fig. 2. It very well may be seen from the figure that the state of variety of μ with energy, for all the examined materials, was like each other; however, every one of them changed by a factor comparing to its physical thickness and chemical content. It is observed that the most elevated μ values over all the photon energy run were found for both compact and cortical bone tissues that credited to moderately high thickness and the plenitude of high atomic number inside their chemical contents.

Table 4. Variation of Linear Attenuation Coefficient of Human Tissues and PMMA for Photon Energies (0.015–2.0) MeV

Energy (MeV)	adipose	Skin	Muscle	Brain	Blood	Lung	Soft	Bone compact	Bone cortical	PMMA
0.015	8.68E-01	1.54E+00	1.63E+00	1.64E+00	1.67E+00	1.67E+00	1.43E+00	1.13E+01	1.55E+01	8.74E-01
0.02	4.47E-01	7.32E-01	7.67E-01	7.69E-01	7.85E-01	7.83E-01	6.80E-01	4.99E+00	6.78E+00	4.60E-01
0.03	2.47E-01	3.45E-01	3.47E-01	3.47E-01	3.54E-01	3.52E-01	3.18E-01	1.68E+00	2.21E+00	2.67E-01
0.04	2.00E-01	2.56E-01	2.50E-01	2.51E-01	2.56E-01	2.54E-01	2.35E-01	8.80E-01	1.09E+00	2.23E-01
0.05	1.82E-01	2.24E-01	2.16E-01	2.16E-01	2.20E-01	2.18E-01	2.05E-01	5.95E-01	6.97E-01	2.05E-01
0.06	1.73E-01	2.08E-01	1.99E-01	1.99E-01	2.03E-01	2.01E-01	1.90E-01	4.68E-01	5.23E-01	1.96E-01
0.08	1.61E-01	1.91E-01	1.81E-01	1.81E-01	1.85E-01	1.83E-01	1.74E-01	3.61E-01	3.80E-01	1.84E-01
0.1104	1.49E-01	1.75E-01	1.66E-01	1.66E-01	1.69E-01	1.68E-01	1.60E-01	3.03E-01	3.07E-01	1.70E-01
0.15	1.37E-01	1.61E-01	1.53E-01	1.52E-01	1.56E-01	1.54E-01	1.47E-01	2.68E-01	2.67E-01	1.57E-01
0.2	1.26E-01	1.48E-01	1.40E-01	1.40E-01	1.42E-01	1.41E-01	1.35E-01	2.42E-01	2.39E-01	1.44E-01
0.3	1.09E-01	1.28E-01	1.22E-01	1.21E-01	1.24E-01	1.23E-01	1.17E-01	2.09E-01	2.06E-01	1.25E-01
0.35	1.03E-01	1.21E-01	1.15E-01	1.15E-01	1.17E-01	1.16E-01	1.11E-01	1.97E-01	1.94E-01	1.18E-01
0.5	8.95E-02	1.05E-01	9.96E-02	9.94E-02	1.02E-01	1.00E-01	9.60E-02	1.71E-01	1.68E-01	1.03E-01
0.613	8.20E-02	9.64E-02	9.13E-02	9.11E-02	9.30E-02	9.21E-02	8.80E-02	1.57E-01	1.54E-01	9.41E-02
0.6616	7.93E-02	9.32E-02	8.83E-02	8.81E-02	8.99E-02	8.90E-02	8.51E-02	1.51E-01	1.49E-01	9.10E-02
1.173	6.04E-02	7.11E-02	6.73E-02	6.71E-02	6.86E-02	6.79E-02	6.48E-02	1.15E-01	1.13E-01	6.94E-02
1.2529	5.84E-02	6.87E-02	6.51E-02	6.49E-02	6.63E-02	6.56E-02	6.27E-02	1.12E-01	1.10E-01	6.71E-02
1.3325	5.66E-02	6.66E-02	6.30E-02	6.29E-02	6.42E-02	6.36E-02	6.07E-02	1.08E-01	1.06E-01	6.50E-02
1.33782	5.56E-02	6.64E-02	6.29E-02	6.28E-02	6.31E-02	6.35E-02	6.06E-02	1.08E-01	1.06E-01	6.49E-02
1.5	5.32E-02	6.26E-02	5.93E-02	5.92E-02	6.04E-02	5.98E-02	5.71E-02	1.02E-01	1.00E-01	6.11E-02
1.6	5.15E-02	6.05E-02	5.73E-02	5.72E-02	5.84E-02	5.78E-02	5.52E-02	9.84E-02	9.68E-02	5.91E-02
1.7	4.98E-02	5.87E-02	5.55E-02	5.54E-02	5.66E-02	5.60E-02	5.35E-02	9.53E-02	9.38E-02	5.72E-02
1.8	4.83E-02	5.69E-02	5.39E-02	5.38E-02	5.49E-02	5.44E-02	5.19E-02	9.25E-02	9.11E-02	5.55E-02
1.9	4.69E-02	5.53E-02	5.24E-02	5.22E-02	5.33E-02	5.28E-02	5.04E-02	8.99E-02	8.86E-02	5.39E-02
2.0	4.57E-02	5.38E-02	5.09E-02	5.08E-02	5.19E-02	5.14E-02	4.90E-02	8.75E-02	8.62E-02	5.24E-02

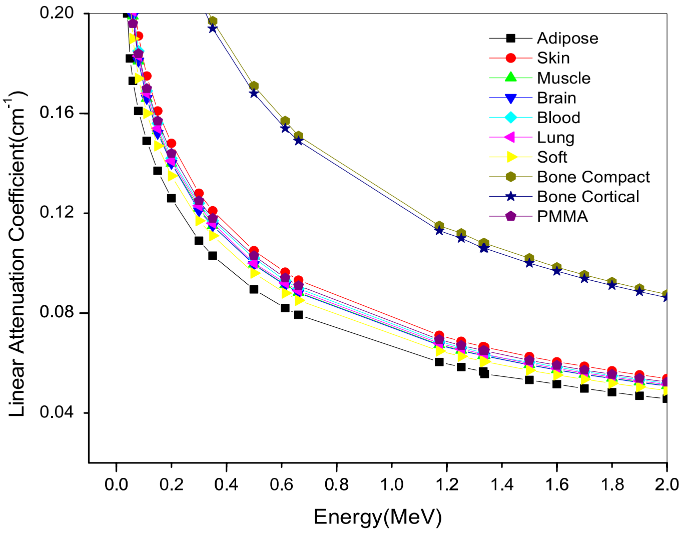

Fig. 2. Variation of linear attenuation coefficient of human tissues and PMMA for photon energies (0.015-2.0) MeV.

To analyse the PMMA as a human tissue substitute, the energy reliance of its μ values is contrasted and that of human tissues as shown in Fig. 3. It is seen from the figure and tables that PMMA has μ estimation of 0.091 cm^{-1} at photon energy of 0.662 MeV, and 0.065 cm^{-1} at photon energy of 1.33 MeV. Then again, blood and lung tissue have μ estimations of 0.0899 and 0.0890 cm^{-1} at photon energy of 0.662 MeV, and 0.0631 and 0.0635 cm^{-1} at photon energy of 1.33 MeV, separately. Their normal μ esteem is 0.0895 with the greatest partial contrast of 1.7 % at 0.662 MeV and normal μ estimation of 0.0633 cm^{-1} with maximum fractional difference of 2.7 % at 1.33MeV. Since the most extreme partial distinction is the smallest between all bends of the gathering of human tissues contrasted with PMMA as a human tissue substitute, which shows that PMMA might be helpful to mimic blood or lung tissue inside the photon energy range under consideration. Likewise, PMMA simulates well muscle and brain tissues inside the considered energy range.

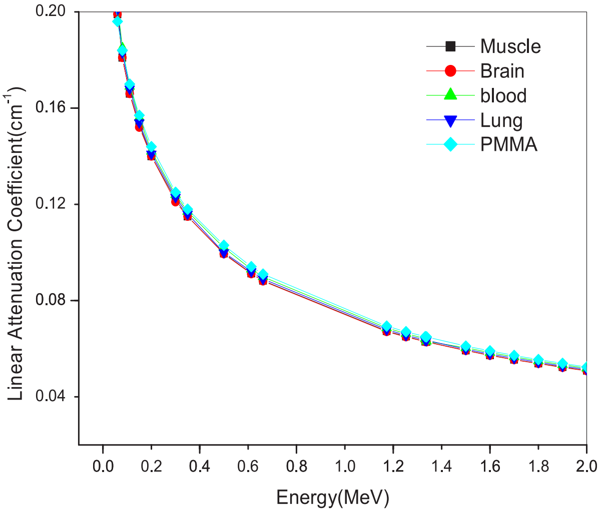

Fig. 3. Variation of linear attenuation coefficient of selected human tissues and PMMA for photon energies (0.015-2.0) MeV.

4. CONCLUSIONS

Brachytherapy is a huge strategy for disease treatment where radioactive fixed sources are used to pass on radiation at a short division by intracavitary, interstitial and surface utilizations. A sensible method to inspect the legitimacy of patient treatment plan, before it is executed, is to gauge dose conveyance around sources, at distances of clinical interest using phantoms incorporating tissue equivalent materials. These materials must have similar radio-physical properties to have the option to re-enact diverse human tissues. To inspect and choose a fitting tissue-equivalent material, the method proposed in this examination includes approval of material tissue comparability. All the radio-physical properties and boundaries related with it should be considered and contrasted with that of the comparing human tissue. In the current work, exhaustive examinations of the gamma-beam attenuation and absorption boundaries have been done for PMMA as a tissue comparable material and the results stood out from that of nine picked human tissues for the photon vitality accommodating in brachytherapy applications. The results showed that the maintenance and disseminate properties of PMMA tissue-equivalent materials depended upon its density, chemical composition and photon energy range. The outcomes additionally proposed that PMMA as a human tissue substitute demonstrated a phenomenal match to muscle, brain, blood, and lung human tissues.

REFERENCES

1. Misra, R., Acharya, S., & Sahoo, S.K. (2010). Cancer Nanotechnology: Application of Nanotechnology in Cancer Therapy. *Drug Discov Today, 15*, 842–850.
2. Verhaegen, F., & Seuntjens, J. (2003). Monte Carlo Modelling of External Radiotherapy Photon Beams. *Phys Med Biol, 48*, 107–164.
3. Palmer, A., Bradley, D., & Nisbet, A. (2012). Physics-Aspects of Dose Accuracy in High Dose Rate (HDR) Brachytherapy: Source Dosimetry, Treatment Planning, Equipment Performance and In Vivo Verification Techniques. *J Contemp Brachytherapy, 4,* 81–91.
4. Yohannes, I., Kolditz, D., & Langner O. (2012). A Formulation of Tissue-and Water-Equivalent Materials Using the Stoichiometric Analysis Method for CT-Number Calibration in Radiotherapy Treatment Planning. *Phys Med Biol, 57,* 1173–1190.
5. Yazdani, M., & Mowlavi, A.A. (2007). Determining TG-43 Brachytherapy Dosimetry Parameters and Dose Distribution for a ^{131}Cs Source Model CS-1. *Iran J Radiat Res*, 5, 85–90.
6. Chandola, R.M., Tiwari, S., & Kowar, M.K. (2010). Effect of In-Homogeneities and Source Position on Dose Distribution of Nucletron High Dose Rate Ir-192 Brachytherapy Source by Monte Carlo Simulation. *J Cancer Res Ther*, *6*, 54–57.
7. Hsu, S.M, Wu, C.H., & Lee, J.H. (2012). A Study on the Dose Distributions in Various Materials from an Ir-192 HDR Brachytherapy Source. *PLoS One, 7,* e44528.
8. ICRU Report No. 44. (1989). *Tissue Substitutes in Radiation Dosimetry and Measurement*. ICRU, Bethesda.
9. Fadhil, F., Abdalsattar, H., & Rajaa, M. (2017). Calculating the X-ray Attenuation Coefficients of Gelatin as Human Tissue Substitute. *Austr J Bas and Appl Sci*, 21–29.
10. Kurudirek, M., & Özdemir, Y. (2011). Energy Absorption and Exposure Buildup Factors for Some Polymers and Tissue Substitute Materials: Photon Energy, Penetration Depth and Chemical Composition Dependence. *J Radiol Prot, 31* (1), 117–28.
11. Gupta, S., & Sidhu, G.S. (2014). Computation of Mass Attenuation Coefficient, Energy Absorption and Exposure Build-Up Factors for Teeth in the Energy Range 0.015–15 MeV up to 40 mfp. *IJETR, 2 (7).*
12. Hopkins, D.N. (2010). *Determination of the Linear Attenuation Coefficient and Buildup Factors of MCP-96 Alloy for Use in Tissue Compensation and Radiation Protection* [Master Thesis]. USA: Ball State University Muncie.
13. Hubbell, J.H, & Seltzer, S.M. (1997). *Tables of X-ray Mass Attenuation Coefficients and Mass Energy-Absorption Coefficients* (version 1.03) (online). Available at http://physics.nist.gov/xaamdi. National Institute of Standards and Technology, Gaithersburg, MD. Originally published as NISTIR 5632, National Institute of Standards and Technology, Gaithersburg, MD.

14. Gerward, L., Guilbert, N., Jensen, K.B., & Levring H. (2001). X-ray Absorption in Matter. Reengineering XCOM. *Rad Phys Chem, 60,* 23–24.
15. Hubbell, J.H., & Seltzer, S.M. (1995). *Tables of X-Ray Mass Attenuation Coefficients and Mass Energy-Absorption Coefficients from 1 keV to 20 MeV for Elements Z ¼ 1 to 92 and 48 Additional Substances of Dosimetric Interest.* Gaithersburg: National Institute of Standards and Technology.
16. ICRP. (2003). *Basic Anatomical and Physiological Data for Use in Radiological Protection* (vol. 89). Reference values. ICRP publication.